

1           **Using Explainable AI and Transfer Learning to**  
2           **understand and predict the maintenance of Atlantic**  
3           **blocking with limited observational data**

4           **Huan Zhang<sup>1</sup>, Justin Finkel<sup>2</sup>, Dorian S. Abbot<sup>3</sup>, Edwin P. Gerber<sup>1</sup>, and**  
5           **Jonathan Weare<sup>1</sup>**

6                                   <sup>1</sup>Courant Institute of Mathematical Sciences, New York University

7                                   <sup>2</sup>Department of Earth, Atmospheric, and Planetary Sciences, Massachusetts Institute of Technology

8                                   <sup>3</sup>Department of the Geophysical Sciences, University of Chicago

9           **Key Points:**

- 10           • Given sufficient training data, convolutional neural networks can predict the main-  
11           tenance of Atlantic blocking from an initial blocked state.
- 12           • Transfer learning from an idealized model to reanalysis data enables predictive skill  
13           in the low data regime of the observational record.
- 14           • Feature importance analysis reveals the influence of upstream flow on blocking per-  
15           sistence and quantifies biases in the idealized model.

---

Corresponding author: Jonathan Weare, [weare@nyu.edu](mailto:weare@nyu.edu)

**Abstract**

Blocking events are an important cause of extreme weather, especially long-lasting blocking events that trap weather systems in place. The duration of blocking events is, however, underestimated in climate models. Explainable Artificial Intelligence are a class of data analysis methods that can help identify physical causes of prolonged blocking events and diagnose model deficiencies. We demonstrate this approach on an idealized quasigeostrophic model developed by Marshall and Molteni (1993). We train a convolutional neural network (CNN), and subsequently, build a sparse predictive model for the persistence of Atlantic blocking, conditioned on an initial high-pressure anomaly. Shapley Additive ExPlanation (SHAP) analysis reveals that high-pressure anomalies in the American Southeast and North Atlantic, separated by a trough over Atlantic Canada, contribute significantly to prediction of sustained blocking events in the Atlantic region. This agrees with previous work that identified precursors in the same regions via wave train analysis. When we apply the same CNN to blockings in the ERA5 atmospheric reanalysis, there is insufficient data to accurately predict persistent blocks. We partially overcome this limitation by pre-training the CNN on the plentiful data of the Marshall-Molteni model, and then using Transfer Learning to achieve better predictions than direct training. SHAP analysis before and after transfer learning allows a comparison between the predictive features in the reanalysis and the quasigeostrophic model, quantifying dynamical biases in the idealized model. This work demonstrates the potential for machine learning methods to extract meaningful precursors of extreme weather events and achieve better prediction using limited observational data.

**Plain Language Summary**

Blocking events are an important cause of extreme weather, especially long-lasting blocking events that trap weather systems in place. The duration of blocking events is, however, systematically underestimated in climate models. Using data generated by a simplified atmospheric model we demonstrate that, given sufficient training data, convolutional neural networks can predict the maintenance of Atlantic blocking from an initial blocked state. Next, we show that first training the neural network on data from the simplified model and then fine tuning the training using real world weather data enables prediction even with few examples of long-lasting blocking events in the observational record. Subsequent feature analysis of the resulting neural networks identifies the input variables that most strongly impact their predictions, revealing that areas of high pressure in certain parts of North America and the North Atlantic Ocean are important for predicting long-lasting blocking events and quantifying biases in the idealized model relative to real weather.

**1 Introduction**

Blocking events are high-amplitude, quasi-stationary anticyclonic high-pressure anomalies that give rise to prolonged abnormal weather conditions in the mid-to-high latitudes (Rex, 1950; Woollings et al., 2018; Lupo, 2021). Blocking events can lead to regional extreme weather by disrupting the usual westerly flow for extended periods (e.g., Kautz et al., 2022), causing extreme heatwaves, floods, and winter storms (e.g., Lupo et al., 2012).

The predictive skill of numerical weather models has improved dramatically, but they still cannot accurately forecast important aspects of blocking events. Blocking frequency and duration are generally simulated poorly by climate models (Davini & D’Andrea, 2020), and even by numerical weather prediction models in medium-range forecasts (Matsueda, 2009; Ferranti et al., 2015; Woollings et al., 2018). Several possible contributing factors have been proposed, including the accuracy of the model’s mean flow (Scaife et al., 2010) or synoptic eddies (Berckmans et al., 2013; Zappa et al., 2014a), the model’s resolution (Davini & D’Andrea, 2016) and subgrid-scale parameterizations (d’Andrea et al., 1998), and even

66 the choice of blocking index itself (Dole & Gordon, 1983; Tibaldi & Molteni, 1990; Pelly  
67 & Hoskins, 2003).

68 Two commonly used blocking indices (Dole & Gordon, 1983; Tibaldi & Molteni,  
69 1990) highlight two essential features of a blocking *event*: (i) a large positive anomaly  
70 of geopotential height that displaces the midlatitude jet, “blocking” the flow, that (ii)  
71 persists for longer than typical synoptic variability. Often a five-day (5d) threshold is  
72 invoked, but the longer the flow remains in a blocked state, the more severe the impli-  
73 cations, either for extended cold/hot conditions or an increased likelihood of compound  
74 storm events (i.e., back-to-back storms, which can dramatically increase the potential  
75 for damage; Kautz et al., 2022). The persistence of blocking is the focus of our study:  
76 given the onset of a blocked state, what is the likelihood that the flow will remain blocked  
77 for an extended period, 5 days for a standard event, or up to 9 days for more extreme  
78 cases? We take a data-driven approach, training a convolutional neural network to iden-  
79 tify persistent blocks at the onset of a blocked state.

80 To understand blocking, various low-order models have been formulated to iden-  
81 tify essential features. In an influential early work, Charney and DeVore (1979) mod-  
82 eled blocking as one of two equilibrium states of a set of dynamical equations for a highly  
83 truncated barotropic channel model. Others used low-order models to propose that the  
84 positive feedback of synoptic-scale eddies on the blocking structure contributes to the  
85 long-time maintenance of blocks (McWilliams, 1980; Hoskins et al., 1983; Shutts, 1983).  
86 While these low-order models have provided useful physical insight, their application to  
87 the real world is limited by lack of land-sea interactions, topography, and other factors.  
88 Comprehensive models, on the other hand, are becoming skillful in simulating realistic  
89 blocking [(e.g. Davini et al. (2021))], but their complexity makes it challenging to iso-  
90 late the essential mechanism(s), and expensive to simulate numerous events.

91 To strike a balance between complexity, transparency, and statistical robustness  
92 from abundant data (model output), we begin with the Marshall-Molteni (MM) model (Marshall  
93 & Molteni, 1993), a three-layer quasigeostrophic (QG) approximation of the atmosphere  
94 that has previously been used to study blocking events (e.g., Lucarini & Gritsun, 2020).  
95 The MM model captures the main features of the northern hemisphere atmosphere rea-  
96 sonably well. For example, Michelangeli and Vautard (1998) found that an enhanced baro-  
97 clinic wavetrain traveling across the North Atlantic is necessary to trigger the onset of  
98 the Euro-Atlantic blocking in both this simple model and reanalysis. They also pointed  
99 out that wave-wave interactions and wave-mean interactions dominate local amplifica-  
100 tion and the propagation of anomalies, respectively.

101 The MM model allows us the freedom to develop and test methods in a data-rich  
102 setting, and precisely quantify the degradation of skill as we pass to a more realistic, data-  
103 poor setting. For the particular application of blocking, here we address the question:  
104 how well can a data-driven method identify persistent events as a function of the input  
105 data you allow it? Furthermore, to gain insight into the physics and predictability of block-  
106 ing, we turn to Explainable Artificial Intelligence (XAI) techniques, following work by  
107 Labe and Barnes (2021) and Rampal et al. (2022). Specifically, we employ Shapley Ad-  
108 ditive ExPlanation (SHAP) analysis to identify key regions upstream of the blocking cen-  
109 ter that enable prediction, and use this to construct low-order models the can be inter-  
110 preted in the context of prior work.

111 Our ultimate goal, however, is to forecast and understand the maintenance of blocks  
112 in our atmosphere, for which we shift the focus to ERA5 reanalysis (Hersbach et al., 2020).  
113 For the most extreme case of a 9-day block in the North Atlantic, only 18 have occurred  
114 in the historical record (See Tab. 3). What chance does a data-driven approach have?  
115 To address the problem of limited data, we apply transfer learning: first we train a con-  
116 volutional neural network on the MM model to learn the basic features of blocking, and  
117 then we re-train it on the limited ERA5 data to calibrate it for the real atmosphere. In

118 this direction our results serve as proof-of-concept. It is likely another choice of phys-  
 119 ical model could strike a better balance between accuracy and simulation cost for our  
 120 purpose. Nonetheless, we find that pre-training on the MM model yields a better pre-  
 121 predictor than when we train the same network on ERA5 alone, proving the efficacy of the  
 122 transfer learning approach.

123 The remainder of this paper is organized as follows. Section 2 introduces the Marshall-  
 124 Molteni (MM) model, training data and blocking index. Section 3 formulates the block-  
 125 ing event criteria and forecasting problem. Section 4 discusses our convolutional neural  
 126 network structure and training details. We first focus exclusively on the MM model in  
 127 sections 5 and 6, applying XAI techniques to visualize the important features for pre-  
 128 diction and testing the results by building a sparse model with features guided by the  
 129 XAI. We also suggest physical interpretations for these predictive features. Finally, we  
 130 turn to the ERA5 data set in Section 7, applying transfer learning to improve the pre-  
 131 diction of persistent blocks in ERA5, especially for more extreme events. SHAP anal-  
 132 ysis shows how transfer learning has modified the CNN to adapt to the new data set,  
 133 but preserves the use of key upstream regions for prediction.

## 134 2 Model and blocking index

135 Marshall and Molteni (1993) developed a 3-layer quasi-geostrophic model of the at-  
 136 mosphere to study atmospheric low-frequency variability. We refer the reader to Appendix Ap-  
 137 pendix A for a complete description. We use a Northern Hemisphere only version of the  
 138 model developed by Lucarini and Gritsun (2020) with 6210 degrees of freedom. The model  
 139 is run with T31 horizontal resolution (corresponding to 90 longitude  $\times$  23 latitude grid-  
 140 points across the northern hemisphere). All model output fields, as well as the reanal-  
 141 ysis used later, are averaged daily.

142 We use an index developed by Dole and Gordon (1983) to define blocking events,  
 143 hereafter referred to as the DG index. This is an anomaly-based blocking index, but has  
 144 been shown to capture the same essential features of blocking as other measures, e.g.,  
 145 that of Tibaldi and Molteni (1990). We compute this index by transforming the spher-  
 146 ical harmonic representation of the streamfunction  $\psi$  at 500 hPa into approximate geopo-  
 147 tential height,  $Z$ , on a Gaussian grid for latitude and a uniform grid for longitude. The  
 148 approximation is the choice of a fixed Coriolis parameter  $f_0$  to convert from  $\psi$  to  $Z$ , which  
 149 causes minimal distortion over our midlatitude area of focus. Blocks are based on de-  
 150 viations of the geopotential height from climatology, denoted  $Z'$ .

151 A *blocking event* is said to occur at a specific location when  $Z'$  stays above a tun-  
 152 able geopotential height anomaly threshold,  $M$ , for at least five consecutive days. In their  
 153 paper, Dole and Gordon (1983) tested statistics for varying  $M$  values, ranging from 50  
 154 m to 250 m, with subsequent studies adopting different thresholds (Chan et al., 2019,  
 155 Tab. 2). For our investigation, we calibrated  $M = 100$  m for our MM model simula-  
 156 tion to roughly match the blocking fraction computed from ERA5 reanalysis data, where  
 157 we used the threshold  $M = 150$  m as in Mullen (1987).

158 Fig. 1 shows the blocking event statistics during the simulation. For comparison,  
 159 blocking event statistics computed from ERA5 reanalysis data from 1959-2021 are also  
 160 shown. In this study, we focus on North Atlantic blockings indicated by the white rect-  
 161 angle in Fig. 1. We pick this region because it has a relatively high blocking frequency,  
 162 and for its important influence on western Europe. We use  $Z_B$ , the average 500 hPa geopo-  
 163 tential height anomaly over this target region over the North Atlantic, to define blocked  
 164 states and blocking events.

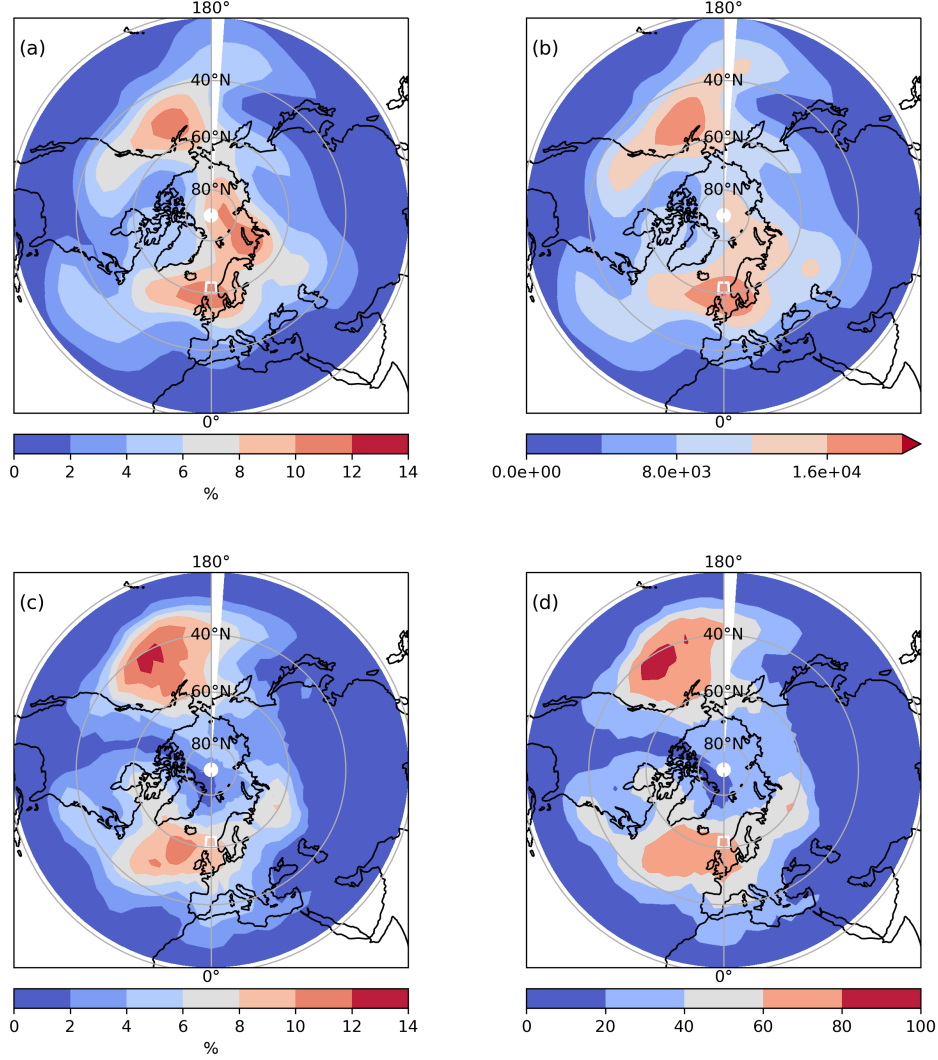


**Figure 1.** (a) Blocking fraction (the percent of days with  $T \geq 5$  days) for MM model data with  $M = 100$  m. (b) total blocking event counts for MM model data during the simulation. (c) blocking fraction for ERA5 reanalysis data with  $M = 150$ . (d) total blocking event for ERA5 reanalysis data with  $M = 150$ m. In all subfigures, the region we focus on is indicated by the white rectangle centered at 0°E and 62°N (approximately spanned by 3 longitude points covering 4°W-4°E, and 2 latitude points covering 60°N-64°N)

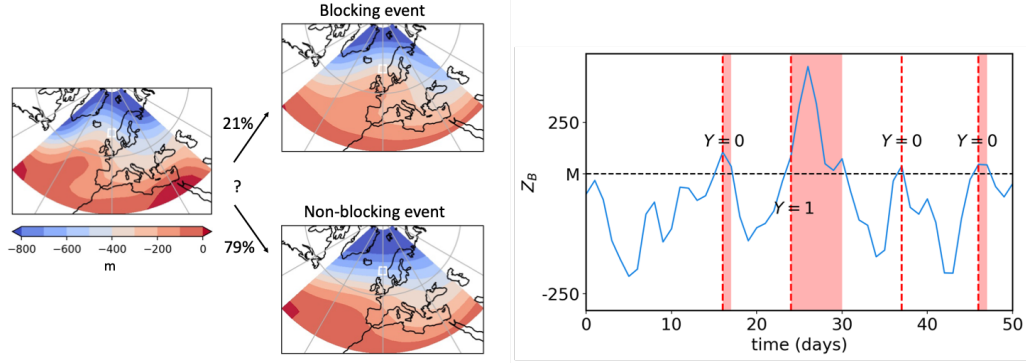


**Figure 2.** Left: The blocking persistence problem: given a nascent blocked state, the goal is to forecast whether it will persist into a long-lasting blocking event, or quickly return to climatology. The percentile represents the climatological probability. Right: A sample trajectory of  $Z_B(t)$ , the anomaly of geopotential height defined in Sec. 2. The vertical dashed lines indicate new blocked states ( $T = 1$ ). The red shading indicates the duration of the block. The label  $Y = 1$  indicates that the blocked state persisted 5 days to constitute a blocking event, while  $Y = 0$  indicates that it did not.

### 3 Probabilistic forecasting and event definition

We aim to study the *maintenance* of blocks rather than their *onset*. Precisely, we formulate the question as the classification problem posed in Fig. 2: given a nascent blocked state, i.e., the state on a day that geopotential height anomalies over the North Atlantic first exceed the threshold  $M$ , can we immediately predict whether the flow will remain blocked for 5 or more days—evolving into a *blocking event*—or will the flow return back towards the climatological state before 5 days have passed? In the MM model, nascent blocked states evolve into 5-day persistent blocking events approximately 21% of the time.

We pose the classification problem: given only the state at the time of blocking onset, can a data-driven method accurately identify the rarer cases that will persist for more than 5 consecutive days? Mathematically, we denote the full model state by  $\mathbf{X}$  and further introduce a variable  $T$  for the running duration of a blocked state:

$$T = (\text{days since } Z_B < M). \quad (1)$$

Note that  $Z_B(t)$  is determined by the state vector  $\mathbf{X}(t)$  at any time  $t$ , but  $T(t)$  retains some memory of previous states and thus is not fully determined by  $\mathbf{X}(t)$ . For example, as shown in Fig. 2, suppose  $Z_B(t)$  first rises above  $M$  on day  $t = 16$  and dips back below  $M$  on day  $t = 18$ . Then,  $T(t) = 0$  for all days through  $t = 15$ ,  $T(16) = 1$ ,  $T(17) = 2$ , and  $T(18) = 0$ . With this notation, we can say that “ $\mathbf{X}(t)$  is the beginning of a blocking event” if

$$T(t) = 1 \quad \text{and} \quad T(t + D - 1) = D. \quad (2)$$

The condition  $T(t + D - 1) = D$  only holds when there are at least  $D$  consecutive days with  $Z_B(t) \geq M$  starting from  $t$ . We can see an example of this in Fig. 2 at day 24, for both a block of duration 5 and 7 d. Here,  $T(24) = 1$ , and  $T(28) = 5$ , triggering the condition for  $D = 5$ . The flow remains blocked through  $T(30) = 7$ , such that day 24 would also count as the onset of a  $D = 7$  day blocking event.

With this formulation, our central question becomes: given a  $T(t) = 1$  state at time  $t$  (the flow has just become blocked), will it stay blocked for  $D$  days,  $T(t + D -$



1) =  $D$ , or not? We address this question by estimating the conditional probability:

$$q(\mathbf{x}(t)) = \mathbb{P}[T(t + D - 1) = D | \mathbf{X}(t) = \mathbf{x}(t), T(t) = 1]. \quad (3)$$

178 Many recent studies have summarized extreme climate and weather events via similar  
 179 functions of state (e.g., Tantet et al., 2015; Finkel et al., 2021; Lucente et al., 2022; Jacques-  
 180 Dumas et al., 2023; Miloshevich et al., 2023). Unless otherwise specified, we adopt  $D =$   
 181 5 to maintain consistency with the common blocking indices (Dole & Gordon, 1983; Tibaldi  
 182 & Molteni, 1990; Pelly & Hoskins, 2003). We also consider more extreme events with  
 183  $D = 7$  and  $D = 9$ .

## 184 4 Convolutional Neural Network Training and Performance

185 Convolutional Neural Networks (CNN) have gained widespread application in prob-  
 186 abilistic forecasting problems (Liu et al., 2016; Ham et al., 2019; Miloshevich et al., 2023)  
 187 for their outstanding performance on multidimensional data sets with spatial structure.  
 188 A CNN differs from a dense neural network in the use of convolutional layers with shared  
 189 weights and biases across layers within the network, designed to extract features that  
 190 exhibit translation invariance across the input space (Goodfellow et al., 2016). Originally  
 191 developed in the context of image processing, CNN excels in scenarios where target ob-  
 192 jects, such as the face of a cat, may appear at different places within the training im-  
 193 age. Convolutional layers allow the network to efficiently learn predictive features, com-  
 194 bining information across multiple images. In our context, we expect predictive contri-  
 195 butions from atmospheric eddies and Rossby waves, which share similar dynamics across  
 196 all longitudes. A CNN can potentially extract these features more effectively than a fully  
 197 connected architecture could, while still learning how they vary with longitude due to  
 198 topography and other zonal asymmetries.

199 The structure of the CNN in this investigation follows Miloshevich et al. (2023) and  
 200 is shown in Fig. 3. It consists of a three-layer architecture, combining convolutional fil-  
 201 ters followed by ReLU activations. Specifically, we use 32 and 64 filters ( $3 \times 3$ ) for the  
 202 first and last two convolutional layers. Between each pair of convolutional layers is a max-  
 203 pooling layer. The output is then flattened and passed to a dense layer with 64 neurons  
 204 that produces 2 outputs. Finally, a softmax function converts these two outputs to com-  
 205plementary probabilities.

206 We performed experiments with alternative CNN structures and found that reduc-  
 207 ing the widths of layers mitigates overfitting, but also reduces the performance at the  
 208 best epoch (not shown). Therefore we adopt the architecture in Fig. 3 and use early-stopping  
 209 to avoid overfitting, as detailed below.

### 210 4.1 Training and Test Datasets

211 We create a training and test set of all states where the flow has just become blocked:  
 212  $\{(\mathbf{X}, T) | T = 1\}$ , where  $\mathbf{X}$  are  $18 \times 90 \times 3$  (latitudes  $\times$  longitudes  $\times$  pressure at levels  
 213 of 200 hPa, 500 hPa, 800 hPa) grid maps of geopotential height from  $20^\circ\text{N}$  to  $87^\circ\text{N}$ . Our  
 214 goal is to classify which of these cases persist into blocking events ( $Y = 1$ ) versus states  
 215 that do not ( $Y = 0$ ). Fig. 2 shows a sample time series with 4 instances of a nascent  
 216 blocked state,  $t = 16, 24, 38$  and  $47$ , only the second of which evolves into a persistent  
 217 blocking event:  $Y = 0, 1, 0$ , and  $0$ , respectively. For each case, the model must clas-  
 218sify  $Y = 0$  or  $Y = 1$  given only  $\mathbf{X}$  at the onset time.

219 We examined the sensitivity of CNN model performance with respect to different  
 220 amounts of training data. To prepare the dataset, we integrate the MM model for 1250k  
 221 days in total. The computational cost is low, requiring 1 CPU core and approximately  
 222 11 hours. We select the first  $n$  days (with  $n$  ranging from 1k to 1000k) to create the train-  
 223ing data set, and always take the last 250k days for the test dataset. Thus all models

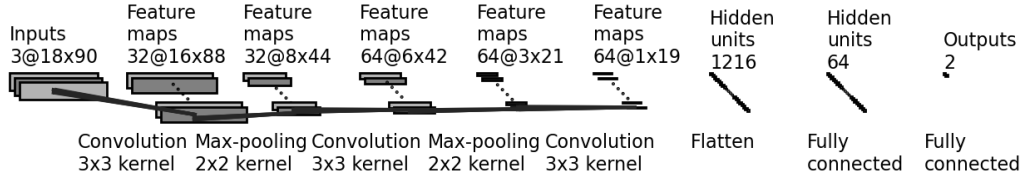


**Figure 3.** Convolutional Neural Network structure. The three convolutional layers respectively use 32, 64 and 64 filters ( $3 \times 3$ ), followed by ReLu activations. Between each pair of convolutional layers is a max-pooling layer with window size  $2 \times 2$ . Then the output is flattened and passed to a dense layer with 64 neurons that produces 2 outputs. A softmax function maps these outputs to two positive numbers between zero and one, representing the estimated probabilities of the the nascent blocked state to persist or decay.

Training data		Test data	
Days	Nascent blocked states	Days	Nascent blocked states
1k	63		
10k	699		
100k	7024	250k	17755
500k	35078		
1000k	70635		

**Table 1.** Length of trajectory (in thousands of days) vs. number of nascent blocking states ( $T = 1$ ) in training set and test sets of varying size.

224 can be fairly compared. The trajectory length and the corresponding number of nascent  
 225 blocked state states are shown in Tab. 1. The likelihood  $q$  of forming a blocking event  
 226 varies depending on different persistence thresholds  $D$ . This dependence relationship is  
 227 illustrated in Tab. 2.

## 228 4.2 Learning procedure

For simplicity, we use binary cross entropy as a loss function, a common choice for classification (Miloshevich et al., 2023). Alternative loss functions have been studied by Rudy and Sapsis (2023). The loss function  $L(q)$  is defined as as follows:

$$L(q) = -\frac{1}{N} \sum_{i=1}^N \left[ Y_i \log q(Y_i = 1) + (1 - Y_i) \log(1 - q(Y_i = 1)) \right]$$

229 where  $q(Y_i = 1) \in (0, 1)$  is the probability of the event  $Y_i = 1$  as predicted by the  
 230 CNN.  $L(q)$  is small when the CNN assigns high probability to positive events and low  
 231 probability to negative events.

232 Given the rarity of blocking events, the data exhibit a pronounced class-imbalance,  
 233 which becomes increasingly severe for longer block durations. As shown in Tab. 2, for  
 234  $D = 5$ , only about 1 in 5 nascent blocked states persist into an event, but  $D = 9$ , less  
 235 than 1 in 20 evolve into persistent events. With this extreme imbalance, a model that



Threshold	$Y = 1$	$Y = 0$	Positive rate
$\geq 5$ d	18748	69642	0.212
$\geq 7$ d	8522	79868	0.096
$\geq 9$ d	3891	84499	0.044

**Table 2.** The statistics of blocking events in our MM 1250k day simulation. The full dataset exhibits 88390 nascent blocking states ( $T = 1$  states).  $Y = 1$  marks the number of these nascent blocks that persist for 5, 7, or 9 d, thus evolving into a blocking event under these respective thresholds, while  $Y = 0$  denotes the number that don’t make it to the threshold.

236 never predicts an event will be correct over 80% or 95% of the time, respectively. How-  
 237 ever, such a model would clearly underperform in terms of precision and recall (defined  
 238 in the next subsection), which would both be zero.

239 To address the class imbalance, for our results in this section we employ over-sampling (Johnson  
 240 & Khoshgoftaar, 2019) techniques during training. In each epoch, we sample an equal  
 241 number of nascent blocks from both classes until we complete an iteration over all the  
 242 nascent blocks in the overrepresented class. As a result, the nascent blocks that persist  
 243 have been sampled multiple times during each epoch.

### 244 4.3 Performance metrics

Throughout this study, we evaluate model performance using two key metrics: *precision* and *recall*. We monitor the values of these metrics on the test dataset throughout the training process to determine the stopping point in order to avoid overfitting. The precision and recall are respectively defined as

$$\text{Precision} = \frac{\text{True positives}}{\text{True positives} + \text{False positives}}, \quad (4)$$

$$\text{Recall} = \frac{\text{True positives}}{\text{True positives} + \text{False negatives}}, \quad (5)$$

245 where “True positives” is the number of data points with  $Y = 1$  for which our CNN  
 246 correctly predicts a persistent blocking event; “False positives” is the number of data points  
 247 with  $Y = 0$  for which our CNN incorrectly predicts a persistent blocking event; and “False  
 248 negatives” is the number of data points with  $Y = 1$  for which our CNN incorrectly pre-  
 249 dicts that the blocked state does not persist.

250 More informally, the precision measures the fraction of *forecasted* persistent blocks  
 251 that *actually* persist. The recall, on the other hand, is the fraction of *actually* persistent  
 252 blocks that are successfully *forecasted*. If one randomly predicts events with the clima-  
 253 tological mean rate  $p$ , regardless of the system state, then the precision and recall are  
 254 both given by  $\frac{p^2 N}{p^2 N + (1-p)pN} = p$ . This sets the floor for a useful predictor: both the pre-  
 255 cision and recall must be higher than the climatological rate.

256 There can be tradeoffs between improving the precision and recall. Predicting the  
 257 event all the time will give you a perfect recall, but climatological precision  $p$ . A low re-  
 258 call implies missing a substantial number of positive events, leading to inadequate prepa-  
 259 ration and increased risk of damage. Conversely, a low precision suggests over-predicting  
 260 events, “crying wolf” too often. In the context of extreme weather forecasting, this can  
 261 lead to over-preparation, consequently reducing the efficiency of regular societal oper-  
 262 ations, as well as trust.

A reasonably high value of both recall and precision is crucial for an effective and resource-efficient forecasting model. We use a simplistic definition of ‘best’ performance, expressed as

$$\text{Overall performance} = \text{Precision} + \text{Recall} . \quad (6)$$

263 However, it is crucial to note that in practical scenarios, designing overall performance  
264 metrics requires careful consideration of the cost of preparing vs. risk of damage asso-  
265 ciated without preparation.

266 This naïve criterion only works when the precision and recall are both reasonably  
267 high, since forecasting the event all the time will yield a performance score of  $1+p$  (re-  
268 call of 1 and precision of  $p$ ). We used caution in ERA5 based forecasts, requiring our trained  
269 models exhibit nontrivial precision above the climatological rate. **We found that the F1-**  
270 **score (Sasaki et al., 2007), another common performance metric, selects the same epoch**  
271 **as the metric in (6).**

#### 272 4.4 Performance and early stopping technique

273 The top row of Fig. 4 shows the precision and recall evaluated on the test data for  
274 varying training data sets for  $D = 5$ . Both the precision and recall metrics are plot-  
275 ted starting from the end of Epoch 1 (the leftmost point on the horizontal axis of Fig. 4);  
276 From Epoch 2 to Epoch 10, the precision increases, chiefly reflecting a decrease in the  
277 false positive rate, as the CNN becomes better at discriminating between persistent and  
278 non-persistent flow configurations. At the same time, the recall slowly decays: the false  
279 negative rate rises slightly as the network becomes more conservative and less likely to  
280 over-predicting persistent cases. Except for the low data regime (1k days), the perfor-  
281 mance of the CNN asymptotes after approximately 10 epochs where the precision and  
282 recall are approximately equal, but this is not necessarily the ideal stopping time (Miloshevich  
283 et al., 2023).

284 **To select the CNN parameters with the best performance, we assessed the over-**  
285 **all performance defined in Eq. (6) at the end of each epoch. We then use the param-**  
286 **eters from the epoch with the largest value.** The “best” CNN is obtained by training on  
287 the full data set of 1000k days for 4 epochs, indicated by the star in Fig. 4. It achieves  
288 precision of 0.70 and recall of 0.87, exhibiting significant predictive power over the cli-  
289 matological mean prediction (the black dashed line with value 0.21). Therefore, we use  
290 it for further analysis in Sec. 5.

291 All of our CNNs significantly outperformed the climatological mean prediction for  
292 any amount of data or training length. Interestingly, although the best performance is  
293 always realized with the longest trajectory of 1000k days, precision and recall have dif-  
294 ferent sensitivities to the training data size. For  $D = 5$  events, the precision improves  
295 with more data up to 100k days (equivalent to approximately 1000 winters), after which  
296 additional data does not lead to much improvement. The recall, however, is more data-  
297 hungry; its performance continues to improve with more data up to 500k days, equiv-  
298 alent to 5 millennia of winter data. This reflects the fact that more data continues to  
299 help the CNN avoid missing events after its ability to limit false positive forecasts has  
300 saturated.

301 Fig. 4 also shows the results for higher persistence thresholds,  $D = 7$  and 9. These  
302 thresholds correspond to rarer events, and even with the longest trajectory of 1000k days,  
303 the precision and recall curves suffer for two reasons. First, as seen from Tab. 2, the num-  
304 ber of positive events drops, effectively limiting the data set almost by a factor of 5 for  
305 the most extreme  $D = 9$  cases. More importantly, however, it simply becomes harder  
306 to discriminate rare events as the data set becomes more imbalanced: less than 1 in 10  
307 nascent blocking states will evolve into a 7 d blocking event, and less than 1 in 20 into

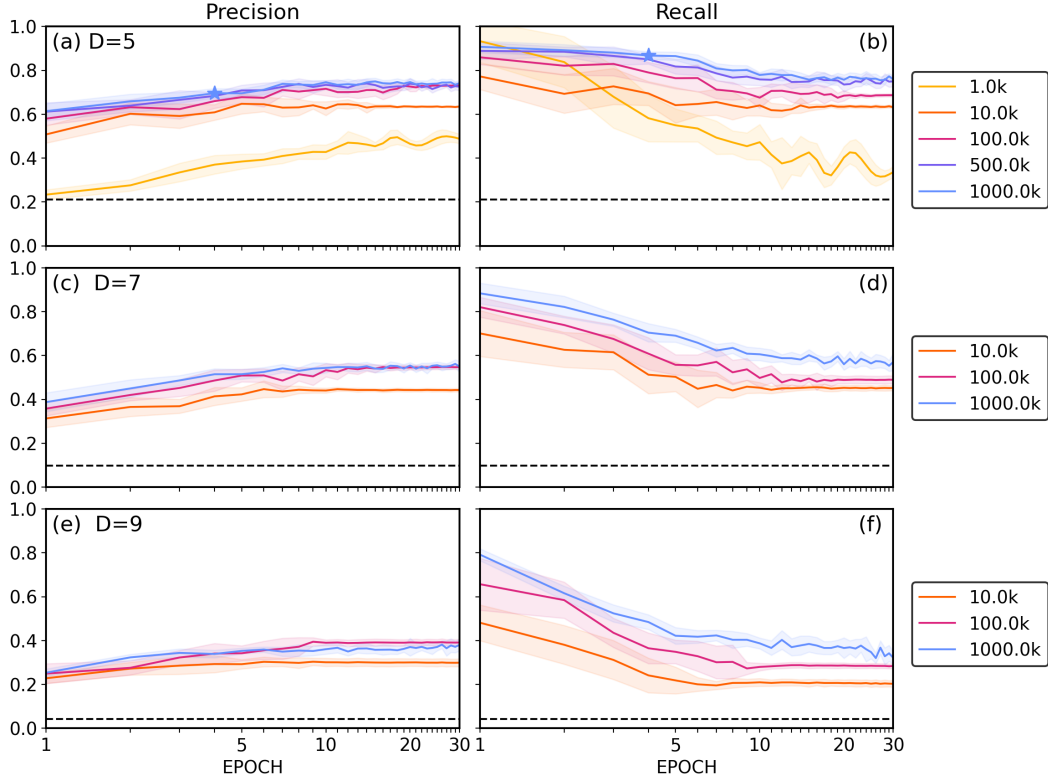


**Figure 4.** Precision (a,c,e) and recall (b,d,f) as a function of training epoch, for CNNs trained on datasets of varying sizes (curve color) and thresholds of blocking persistence (rows). As detailed in the text, all the models are tested on events from the same 250K dataset not seen in training. Panels (a,b) show results for 5 day blocks ( $D=5$ ); for example, the light blue curves are trained on all events in the full 1000k-day simulation, while the other curves show results based on smaller training sets as indicated by the legend. The blue stars indicate the “best” CNN (see text), with a precision=0.70 and recall=0.87. Panels (c,d) show results for  $D=7$  blocks and (e,f) for  $D=9$  blocks. Fewer curves are displayed for  $D = 7$  and  $D = 9$  for the sake of clarity. Shading indicates uncertainty, assessed by taking one standard-deviation of results of ten neural network training with i.i.d random parameter initialization.

a 9 d blocking event. Without our efforts to overcome this imbalance, a network can classify almost all events correctly by never predicting a persistent case.

Despite the difficulties, the CNNs still show some skill in rare event forecasting. Given the full 1000k dataset, for  $D = 9$  the precision and recall converge to about 0.35, a factor of two worse than the CNN in the  $D = 5$  case but a factor of 10 better than climatology. As with the  $D=5$  cases, we found that the recall for  $D = 7$  and 9 suffers more than the precision when the data set shrinks: with less events to learn from, the CNNs become more conservative and less likely to call an event. The recall depends on the false negative rate, and thus appears more sensitive to class imbalance. More data gives the network more true positive cases to learn from, apparently helping to overcome this challenge.

The low precision and recall values for smaller data sets (1k and 10k) do not bode well for training our CNN on ERA5 data, which will be discussed in detail in Section 7. For  $D = 5$ , there are 273 nascent blocked states in the ERA5 record, 84 of which persist into blocking events (see Table 3). This data amount falls between our 1k and 10k cases where data clearly limit performance. Consistent with our experience with the MM model, recall is the metric that suffers most from limited data, and stands to benefit the most from transfer learning.

## 5 Feature analysis: What is our CNN using to predict blocking events?

Before turning to forecasting in the realistic data regime, we ask what our best CNNs have learned to make these forecasts. Explainable Artificial Intelligence (XAI) is an array of techniques used to try to gain some understanding of the basis on which neural networks make predictions (Linaratos et al., 2020). In this section, we use SHapley Additive exPlanation (SHAP) value analysis to dissect the contributions of different atmospheric pressure levels and geographic areas that our CNN is using to make its predictions. We further construct a sparse model using the identified important features as inputs to quantitatively justify their relative importance in the prediction process.

### 5.1 XAI Method

SHapley Additive exPlanation (SHAP) values, introduced by Lundberg and Lee (2017) and Shrikumar et al. (2017), draw inspiration from Shapley values in game theory (Lipovetsky & Conklin, 2001). In the domain of weather and climate science, SHAP values have found broad use, with applications ranging from Earth System model error characterization (Silva et al., 2022) to drought forecasting (Dikshit & Pradhan, 2021).

Intuitively, given a function  $f : \mathbb{R}^d \rightarrow \mathbb{R}$  (such as the conditional probability  $q$  in Eq. 3), SHAP assigns an importance value  $\phi_i$  to each feature  $x_i$  of the argument  $\mathbf{x} \in \mathbb{R}^d$ , which combine additively:

$$f(\mathbf{x}) = \mathbb{E}[f(\mathbf{x})] + \sum_{i=1}^d \phi_i(f, \mathbf{x}). \quad (7)$$

With no knowledge of  $\mathbf{x}$ , the optimal prediction of  $f$  (in a mean-square sense) is the climatological average over the distribution of  $\mathbf{x}$ :  $\mathbb{E}[f(\mathbf{x})]$ . SHAP values quantify how much is gained beyond this baseline by incorporating information from each component  $i$  of  $\mathbf{x}$ . The SHAP values  $\phi_i(f, \mathbf{x})$  are unique for each sample of  $\mathbf{x}$ , but features  $i$  for which  $|\phi_i(f, \mathbf{x})|$  are large for most  $\mathbf{x}$  (that is, a large average SHAP value) can be singled out as important, or useful, for the prediction of  $f(\mathbf{x})$ . SHAP values possess advantageous theoretical properties as well, and we refer the reader to Lundberg and Lee (2017) for a detailed theoretical analysis. In this study, SHAP values are computed using the Python package DeepSHAP (Chen, 2022). The function  $f(\mathbf{x})$  is taken as the estimated conditional

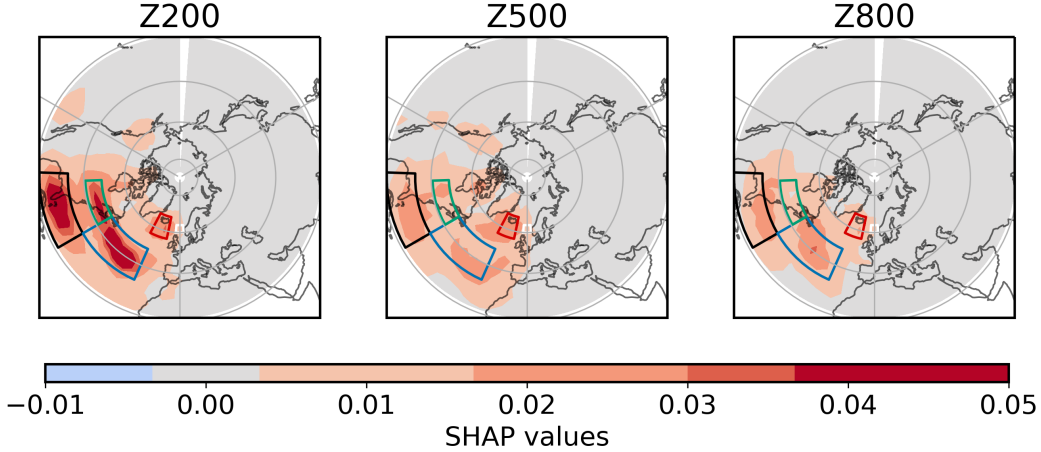


**Figure 5.** Composite maps of SHAP values,  $\bar{\phi}$ , of geopotential height at 200, 500, and 800 hPa, for true positive cases, i.e., when the CNN accurately forecasts a persistent blocking event. The unit is the probability per feature ( $Z$  at a given location and pressure level) of a positive forecast (see equation 7), indicating the feature’s average incremental contribution to the CNN’s confidence that the nascent blocked state will evolve into a persistent blocking. The boundaries of the most important regions learned by the CNN are marked by solid lines and denoted region 1 (Florida, black), region 2 (north Atlantic, blue), region 3 (northeastern North America, green) and region 4 (Iceland, red) .

350 probability  $\hat{q}(\mathbf{x})$  computed by the CNN, i.e., the probability, according to the CNN, that  
 351 the blocked state will extend  $\geq D$  days, leading to a blocking event.

352 **5.2 Results**

353 Fig. 5 shows the composite of SHAP values for true positive data. Because few nascent  
 354 blocks persist for  $D = 5, 7, \text{ or } 9$ , the climatological probability of a persistent event  $\mathbb{E}[\hat{q}(\mathbf{x})] =$   
 355  $0.21, 0.096, \text{ and } 0.044$ , respectively. For our CNN to call a positive event, we require the  
 356 conditional forecast probability  $\hat{q}(\mathbf{x})$  to be larger than 0.5. Hence a positive (negative)  
 357 value of  $\phi_i(\hat{q}, \mathbf{x})$  indicates that knowing the geopotential height anomaly at this level and  
 358 location increases (decreases) the likelihood of a positive event. Therefore, the shading  
 359 in Fig. 5 can be interpreted as the average influence of each grid point for the CNN to  
 360 successfully predict a long-lasting blocking event. **For the averages over each region, the**  
 361 **standard deviations for Z200, Z500, and Z800 are 0.039, 0.026, and 0.028, respectively,**  
 362 **with a roughly symmetric distribution, indicating that the SHAP value analysis in Fig.**  
 363 **5 represents the overall sample behavior, rather than being skewed by outliers.**

364 The SHAP composite is approximately uniformly non-negative because it is based  
 365 only on true positive events: additional information should always increase the forecast  
 366 probability. This indicates that the CNN has been well-trained to only use geopotential  
 367 height information that improves the blocking event probability, and suggests it has iden-  
 368 tified robust features that herald a persistent block. A composite based on true nega-  
 369 tive cases (not shown) reveals similar patterns, but of the opposite sign.

370 The first thing to notice is that anomalies upstream from the blocking region (to  
 371 the west) are more valuable than other regions for predicting the persistence of the blocked  
 372 state. Moreover, the commonality among different pressure levels reflects the relatively

373 barotropic nature of the MM model. In general, however, the CNN prediction relies most  
374 on the upper level flow (200 hPa).

375 The SHAP values emphasize four distinct regions in a quadrupole arrangement to  
376 the west of the Atlantic blocking region, as marked in Fig. 5. We chose these regions to  
377 encapsulate high SHAP values using the following algorithm: after objectively identi-  
378 fying regions where SHAP values exceeded a set threshold, we defined boundaries by hand  
379 with the goal of enclosing these regions across all three levels within the smallest encom-  
380 passing rectangle. While part of the goal of choosing these regions was to build a sparse  
381 predictor in the next section, they give us physical insight on their own.

382 The meaning of the SHAP values can be more easily interpreted with the aid of  
383 composites of the 3341 true positive events (Fig. 6), which show us the sign of anoma-  
384 lies that favor persistence. Positive geopotential anomalies in region 1 (black, centered  
385 over Florida) and 4 (red, over Iceland, just east of the blocking region itself) at the on-  
386 set of blocking indicate to the CNN that a block will persist, while negative anomalies  
387 over Regions 2 (blue, North Atlantic Ocean) and 3 (green, northeast US) also favor per-  
388 sistence.

389 Regions 2 and 4 project onto opposing centers of action of the North Atlantic Os-  
390 cillation (NAO). They indicate that a more negative NAO state at the onset of block-  
391 ing increases the likelihood of a persistent block. Previous studies have also found that  
392 blocks tend to be more persistent when the NAO is negative (Barnes & Hartmann, 2010).  
393 While a blocking pattern off Europe projects weakly onto the NAO itself, SHAP anal-  
394 ysis indicates that the wider structure of the pattern is important. Regions 1, 3, and 4,  
395 on the other hand, appear to be part of a wave train arching southwest from the block-  
396 ing region. Their importance suggests that downstream development of a wave packet  
397 propagating along the jet stream helps drive persistent blocking events in the North At-  
398 lantic.

## 399 6 Building a sparse model with logistic regression

400 In quantifying the relative importance of the geopotential height as a function of  
401 location, the SHAP values suggest there is potential for dimension reduction. The CNN  
402 did not rely significantly on the information about  $Z$  in the large grey regions downstream  
403 of our target blocking area in Fig. 5 to predict the potential persistence of a nascent block-  
404 ing anomaly. Intuitively, conditions over central Asia will take some time to affect the  
405 flow over the North Atlantic, and are mostly irrelevant for a forecast at 5 day range.

406 To gain more physical insight into the utility of the SHAP values, and so gain con-  
407 fidence in our CNNs, we explored a simplistic dimension reduction approach focused on  
408 the regions highlighted in Fig. 5. Our aim was not to achieve the ideal dimension reduc-  
409 tion, but to provide physical insight. Thus we ask: how well can one predict the persis-  
410 tence of a nascent block given only the very coarse information about the flow provided  
411 by the average geopotential height within these regions at the three levels?

412 For these simple models, we computed the local mean of  $Z_{200}$ ,  $Z_{500}$ , and  $Z_{800}$   
413 for each of the four rectangles shown in Fig. 5, resulting in 12 time series. We then ap-  
414 plied logistic regression with all possible combinations of these 12 features for subsets  
415 of dimension up to 5, i.e., for dimension 1, fitting a logistic function with each time se-  
416 ries alone, for dimension 2, all possible combinations of two time series, and so forth. The  
417 results for the sparse models with the best predictive skill on the test set are illustrated  
418 in Fig. 7(a). The horizontal axis denotes the combinations of variables that achieve the  
419 predictive scores shown in the figure.

420 We draw three key conclusions from Fig. 7(a). First, to predict the persistence of  
421 a blocked state, the best one-dimensional feature is  $Z_{200}$  in region 1, over Florida and



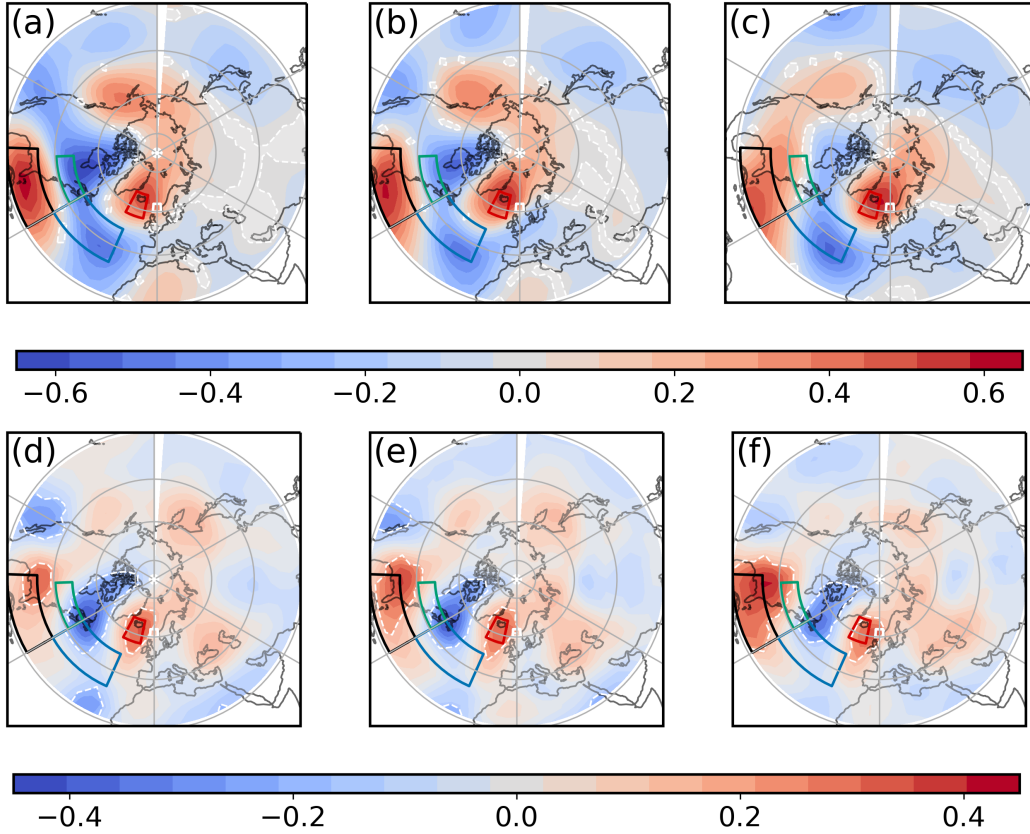


**Figure 6.** Averages of nascent blocking states that evolve into persistent blocking events ( $T = 1, y = 1$ ) of (top row, a-c) MM dataset and (bottom row, d-f) ERA5. The colorbar represents values of geopotential height anomalies normalized by the standard deviation at each location and height. The white dashed line indicates the 0.05 significance level for a one sample  $t$ -test of the null hypothesis that the expected value is zero. The box areas identified by SHAP analysis lie in statistically significant regions. Regions that are not significant are shaded by white. For MM model dataset (the top row), most of the regions are statistically significant, while for ERA5 dataset (the bottom row) most of the regions are not statistically significant.



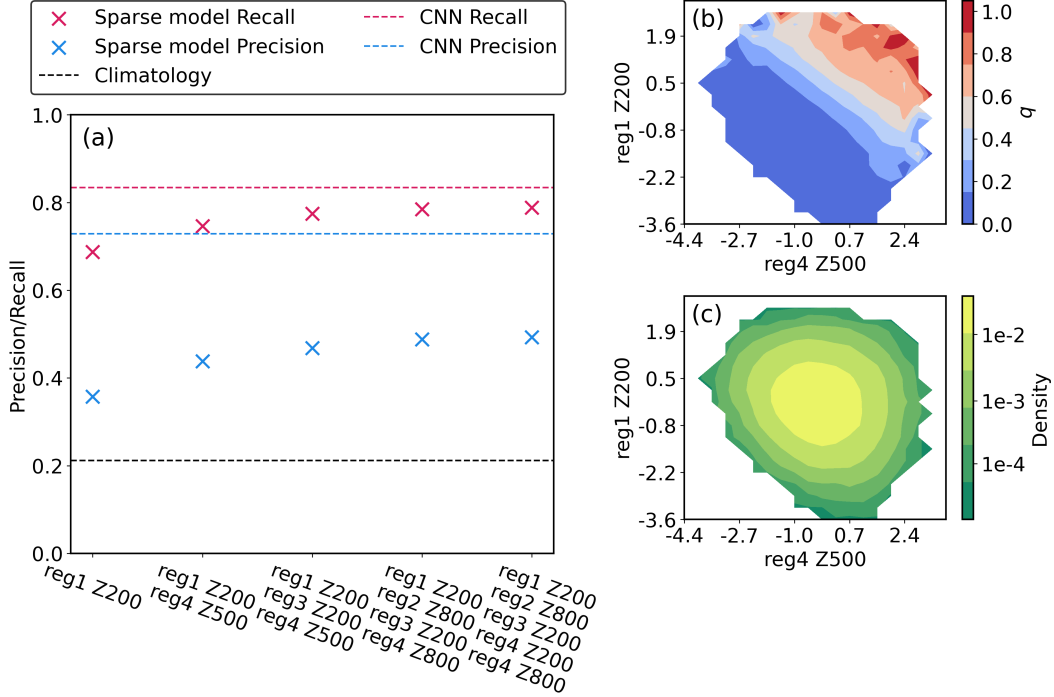


**Figure 7.** (a): Sparse model predictive skill on the test data set. The horizontal axis represents the dimension  $d$  of the sparse model from 1 to 5, with labels showing the combination of variables (“R1” = “region 1”) that achieves the best predictive skill among all combinations of  $d$  variables. (b) Conditional probability of a persistent block,  $q$ , as a function of mean normalized geopotential height anomaly at 200 mb over region 1 and at 500 mb over region 4 (the second column of (a)). (c) The marginal density (likelihood of observing these anomalies) as a function of the same variables. Densities below  $10^{-5}$  are cut off.

422 the Gulf and upstream of the block, not Z500 in region 4, the  $Z$ -field nearest to the block.  
 423 Second, the combination of Z200 in region 1 with Z500 in region 4 forms a two-dimension  
 424 model (shown in Fig. 7(b)) that already recovers a recall value of 0.75—it captures three  
 425 quarters of all blocking events—with a precision of 0.44, twice the climatological rate.  
 426 The precision and recall of the full CNN, however, are 0.87 and 0.70. This leads us to  
 427 the third key message: there is a large discrepancy in precision between CNN and logis-  
 428 tic regression. Even with 5 predictors, the precision of our sparse model is only 0.5.

429 The poor precision indicates that the sparse model makes too many false positive  
 430 predictions. This could suggest that the decay of the Atlantic blocked state is a more  
 431 nonlinear dynamical phenomenon, which cannot be modeled as a simple linear statisti-  
 432 cal model. A CNN can capture these nonlinearities more effectively than sparse regres-  
 433 sion, which is consistent with previous research which found North Atlantic blocks are  
 434 associated with nonlinear processes (Evans & Black, 2003). It could also indicate that  
 435 more subtle features outside these 4 centers (and variation within these regions) are im-  
 436 portant. Fig. 5 indicates that the CNN uses information across all of the North Atlantic,  
 437 eastern North America, and even off the west coast of the US, to make skillful predic-  
 438 tions.

439 To explore the effectiveness of the two-dimensional sparse model, we visualized the  
 440 conditional probability of a block persisting,  $q$ , projected onto this simple subspace (shown  
 441 in Fig. 7(b)). For example, the lightest pink region, corresponding to  $q \approx 0.5$  indicates

442 that if, at the onset of blocking,  $Z$  at 200 hPa over region 1 (Florida) is particularly high  
 443 or  $Z$  at 500 hPa in region 4 (Iceland) is abnormally high, the system has a roughly 50%  
 444 chance of evolving into a persistent block, more than double the climatological rate of  
 445 21%. In the red region at the top right, where both of these regions exhibit abnormally  
 446 high pressure, the chance of a persistent block increases to near 100%.

447 Fig. 7(c) shows the likelihood of observing these  $Z_{200}$  and 500 anomalies. Most of-  
 448 ten, the system exists in the middle of the diagram, where the probability of a blocking  
 449 event hovers near or below the climatological value. The most likely state that exhibits  
 450 a high chance of a block lies along the diagonal from the upper left to the lower right,  
 451 with moderately high  $Z_{200}$  and 500 anomalies. The states in the top right corner, for  
 452 which a persistent block is nearly certain, are very rare.

453 The sparse models suggest physical links between blocking events and the upstream  
 454 flow. The Atlantic blocking region lies at the end of the Atlantic storm track (Michelangioli  
 455 & Vautard, 1998). Persistent blocks, at least in the MM model, are favored when there  
 456 is enhanced wind off the east coast of the US (high pressure over Florida, region 1) and  
 457 low pressure over regions 2 and 3 (which are highlighted in the higher dimensional sparse  
 458 models). This displaces the climatological winds upstream of the blocking region equa-  
 459 torward. This will modify the input of storm activity into the blocking region, consis-  
 460 tent with prior studies that have highlighted the relation between the storm track and  
 461 blocking events (Zappa et al., 2014b; Yang et al., 2021).

## 462 **7 Extending to ERA5 using Transfer Learning**

463 Given sufficient data, it was possible to construct a CNN that skillfully forecasts  
 464 the maintenance of blocking events in the MM model. However, the ERA5 data from  
 465 December, January and February (DJF) between 1940-2022 exhibit only 273 nascent blocked  
 466 states in our Atlantic region of focus. Unfortunately, this low-data regime is where we  
 467 see a significant degradation in performance in Fig. 4. The curve associated with the tra-  
 468 jectory of 10k days (699 nascent blocked states) plateaued at lower values for both the  
 469 precision and recall. With only 1k days (63 nascent blocked states) performance was poor,  
 470 and the learning unstable, oscillating significantly across epochs.

471 The class imbalance between  $Y = 0$  and  $Y = 1$  adds to the difficulty (see Tab. 3),  
 472 particularly when longer blocks are considered. An extreme example is the set of block-  
 473 ing events that last  $\geq 9$  d: there are only 18 such events in the reanalysis record out of  
 474 273 data points. Such a small sample of positive data can hardly support any meaning-  
 475 ful training, and makes it impractical to get meaningful uncertainty bounds on perfor-  
 476 mance. In a standard training-test data split with a ratio of 90:10, only around 2 pos-  
 477 itive events typically fall in the test set, making it challenging to robustly assess the skill.

478 When training on the limited number of events in the reanalysis, a CNN can more  
 479 easily suffer from overfitting, where the network uses ‘noise’ (unrelated features) to clas-  
 480 sify blocking events. Overfitting can be diagnosed when the performance on the test set  
 481 diverges from the training set. Yang and Gerber (submitted) found that the oversam-  
 482 pling strategy used so far in this study was more prone to overfitting than a weighted  
 483 loss function strategy (Johnson & Khoshgoftaar, 2019). With this latter strategy, one  
 484 emphasizes the rare class (in our case, positive events) by increasing its weight in the loss  
 485 function. In our remaining experiments, we weighted positive and negative events inversely  
 486 to their occurrence rate.

### 487 **7.1 Direct training**

488 The scarcity of events makes direct training (DT) on ERA5 blocks challenging. In  
 489 our study of the MM model data, we had the luxury of a large test data set (which we

Threshold	$Y = 1$	$Y = 0$
$\geq 5$ d	84	189
$\geq 7$ d	36	237
$\geq 9$ d	18	255

**Table 3.** The statistics of ERA5 dataset in 1940-2022 DJF with  $T = 1$ .

490 intentionally kept the same for fair comparison of the different CNNs), even for the case  
 491 with only 1k training days. For ERA5 data, we use cross validation (Goodfellow et al.,  
 492 2016) to make the best use of the smaller dataset. The limited number of states were  
 493 partitioned into training and test sets in ratios of 90:10; we also tried 80:20, and the re-  
 494 sults were similar (not shown). These splits were chosen to balance two difficulties: a small  
 495 training set can prevent robust learning, while a small test data set limits accurate eval-  
 496 uation, even for a well-trained model.

497 To proceed, we first reduced the resolution of the ERA5 data to a comparable size  
 498 of the MM output, considering geopotential height on the same three levels at the same  
 499 coarse resolution. Reducing the resolution allowed us to use the same CNN architecture,  
 500 and made transfer learning possible (as discussed below). It also helped avoid overfit-  
 501 ting, reducing the number of input variables relative to the number of events. Then we  
 502 created the test-train splits, yielding 10 cross validation sets with distinct test events.  
 503 Finally, for each test-train split, we trained and evaluated 10 CNNs, where variations were  
 504 confined to random weight initialization and shuffling of training data.

505 Providing meaningful uncertainty on the precision and recall statistics from direct  
 506 training, shown in the left column of Fig. 8, is challenging. As the 10 CNNs trained on  
 507 each train-test split are not independent and identically distributed (IID), we first av-  
 508 erage the skill scores within each split. The 10 test sets, however, can be viewed as IID  
 509 samples. The solid lines and shades respectively represent the mean and two-standard  
 510 deviation bounds of the precision and recall, as a function of epoch, across the 10 splits.

511 For 5 d blocks, a CNN trained by DT can beat the climatological forecast, albeit  
 512 only modestly. Given the small testing data set (27 nascent blocks, of which roughly 8  
 513 persist into events), it is important not to put too much stock in the best possible per-  
 514 forming network, for CNN can get lucky on a small sample size. The average performance  
 515 quantifies the potential skill more reliably. On average, a CNN can achieve a precision  
 516 of approximately 0.45: when it calls a persistent blocking event, 4-5 out of 10 times it  
 517 is correct, as compared to about 3 of 10 in the climatology. The recall was modestly bet-  
 518 ter, the network only missing 4 of 10 actual events, while a climatological forecast would  
 519 miss 7 of 10.

520 We also explore 7 d events, where only 13% of nascent blocks evolve into 7+ d events.  
 521 Again, the average CNN modestly beats the climatological forecast in terms of precision:  
 522 1/5 of the cases it calls evolve into persistent events, roughly double the success rate by  
 523 a guess with a Bernoulli random variable. The recall was initially deceptively high (the  
 524 network captured 5 of 10 blocks), but this skill rapidly decreased with training. This was  
 525 due to the fact that CNNs at early stages of DT call too many events. As it trains fur-  
 526 ther, it reduces the forecast rate, declaring fewer false positives at the expense of miss-  
 527 ing more events.

528

## 7.2 Transfer learning

529

530

531

532

533

Transfer learning (TL) has found broad application in atmospheric science, such as detecting gravity waves (González et al., 2022), improving extreme heatwave forecasts in climate models (Jacques-Dumas et al., 2022), subgrid-scale turbulence parameterization (Subel et al., 2021), image restoration (Guo et al., 2022) and parameter retrieval from raw dew point temperature profiles (Malmgren-Hansen et al., 2018).

534

535

536

537

538

539

540

541

TL involves pre-training a model on a larger dataset that is similar to the dataset of interest (source domain), then fine-tuning the model on the smaller target dataset (target domain). This approach is particularly beneficial when labeled data for the target task is limited, as it allows the model to exploit learned features and representations from the larger dataset to enhance its performance on the smaller dataset. With this strength, TL has shown its power in forecasting, combining the data from a climate model (Rasp & Thuerey, 2021) or a dynamical model (Mu et al., 2020) with the observational record to improve medium-range weather forecasting and ENSO prediction.

542

543

544

545

546

547

548

549

550

551

552

In this section, we apply TL to leverage our MM dataset to predict events in the reanalysis data. As a quasi-geostrophic model, MM has complexity between full climate models (e.g., Rasp & Thuerey, 2021) and low order models (e.g., Mu et al., 2020) used in previous transfer learning studies. The overall process is to first ‘pre-train’ a CNN on the MM model dataset, learning to capture the characteristic features of blocking. While significantly simplified, the MM model is skillful in representing atmospheric variability (Lucarini & Gritsun, 2020), but more importantly provides extensive positive and negative cases to learn from, supporting optimal CNN training, as demonstrated in Sec. 4. After pre-training, our CNN is then fine-tuned on the ERA5 dataset, where the weights are modified to account for biases in the MM model, and the parameter scales are calibrated.

553

554

555

556

557

558

559

560

In most applications of TL, only the weights in the last few layers of a neural network are fine-tuned on the target domain (Yosinski et al., 2014; Hussain et al., 2019; Talo et al., 2019). Following this convention, we only retrain the last layer of the CNN on ERA5 while keeping the other layers frozen. This allows the CNN to correct biases it inherits from MM, but not to fall back into the poorly constrained limit we reached with direct training. We also tried retraining other single layers, but retraining the last layer performed the best. To avoid overfitting, we set the learning rate to 1/10 the learning rate of pre-training.

561

562

563

564

565

566

567

568

569

570

We tested different lengths of pre-training and then evaluated the performance of the resulting models with the peak precision and recall in the transfer-learning phase. The results show that CNN parameters taken at earlier pre-training epochs show better peak performance after transfer learning (results not shown). This suggests that overfitting on the source domain cannot be fully corrected by fine-tuning on the target domain. For the displayed results in Figs. 8, 9 and 10, we use a pre-training of 2 epochs for  $D = 5$ , and 1 epoch for  $D = 7$ . Given the 1000k days of MM integration we had at our disposal, this means that the neural network has explored more than 70,000 unique nascent blocking states (all of them twice, for  $D = 5$ ) before seeing any of the 273 events in ERA5.

571

572

573

574

575

576

577

We follow a similar procedure as with DT to assess the ensemble-average performance. We pre-train 10 CNNs with the 1000k-day MM dataset; the only differences are due to randomness in the initialization and training data shuffling. We then carry out a 10-fold cross-validation procedure with 90:10 splits: for each split, we perform TL fine-tuning on the 10 pre-trained CNNs. We compute the mean precision and recall for each split. The results in the TL columns of Fig. 8 show the mean and 2-standard deviation bounds across all the splits.

578 Compared to DT, TL begins with a higher precision but lower recall due to pre-  
 579 training. With additional fine-tuning, the precision stays almost unchanged, while the  
 580 recall grows markedly. The network is able to increase the number of events that it can  
 581 capture (lowering the number of false negatives) with minimal degradation in reliabil-  
 582 ity of its forecast (that is, only slightly increasing the false positive rate).

583 Uncertainty in the precision is dominated by differences in the true positive events  
 584 between the splits; consequently, the 2-standard deviation error bounds are compar-  
 585 able for DT and TL. The recall is less sensitive to differences among the splits, however,  
 586 and at least for the  $D = 5$  case, there is noticeably less spread across the splits with  
 587 transfer learning. This is understandable because recall, by definition, doesn't depend  
 588 on the positive rate of the test dataset, which varies a lot for small data sets (around 27  
 589 states in each test set after splitting). On the other hand, precision relies on the posi-  
 590 tive rate of the test dataset, so it has more intrinsic variability.

591 We still evaluate the overall performance by Eq. (6). Focusing first on  $D = 5$  events,  
 592 the best mean performance with DT is a precision of 0.45 and recall of 0.61, which is re-  
 593 alized at Epoch 3. With TL, we achieve an average performance with a similar preci-  
 594 sion of 0.45 and higher recall 0.82 (at Epoch 4). A noticeable advantage of TL is the sig-  
 595 nificantly reduced variance in recall compared to DT, indicating TL's superior robust-  
 596 ness in prediction, attributed to its enhanced capacity for capturing predictive features.  
 597 For  $D = 7$  day events, the best mean performance with DT is a precision of 0.21 and  
 598 recall of 0.48, achieved after 3 epochs. TL, however, achieves a precision of 0.22 and re-  
 599 call of 0.76 at Epoch 6.

600 To ensure that these gains in recall are statistically significant, we conducted a Wilcoxon  
 601 signed-rank test (Conover, 1999). Fig. 9 shows histograms of the difference in precision  
 602 and recall between direct training and transfer learning. For example, each of the 10 val-  
 603 ues in the histogram for  $D = 5$  is defined for a specific train-test split, evaluated by sub-  
 604 tracting the mean precision (recall) of 10 randomly initialized TL models taken at Epoch  
 605 4 from the mean precision (recall) of 10 randomly initialized DT models taken at Epoch  
 606 3. The spread here stems primarily from the fluctuation in 10 small-size test sets, not  
 607 uncertainty in the networks due to randomness in training. The values for small-size test  
 608 sets are taken at the same epoch of the best mean performance.

609 The average recall with TL surpasses that of DT by 34% ( $p = 0.001$ ) for 5 d events  
 610 and by over 50% ( $p = 0.002$ ) for 7 d events. While there is not a significant difference  
 611 between the TL and DT precision, it is critical that transfer learning was able to improve  
 612 the recall without sacrificing precision. One could easily inflate the recall by declaring  
 613 more positive cases, but without any skill, the precision would suffer and approach the  
 614 climatological rate.

### 615 7.3 What has transfer learning learned?

616 When we show ERA5 events to CNNs first trained on the MM dataset, what ex-  
 617 actly is the CNN learning to improve the recall? For example, do the key geographical  
 618 regions and levels (Fig. 5) retain the same level of significance? It is reasonable to ex-  
 619 pect that this might not be the case. In the MM dataset, the duration of the Atlantic  
 620 blockings could be related to upstream flow, specifically to the structure of the wave train  
 621 at the blocking onset. The mechanism for blocking in the real world is more complicated,  
 622 and the correlated pattern may shift, intensify, and/or weaken. To address these ques-  
 623 tions, we compare the SHAP values of the pre-trained CNNs when directly applied to  
 624 ERA5 (i.e., without fine-tuning) to the SHAP values of the CNN after 4 epochs of fine-  
 625 tuning, as shown in row *a* and row *b* of Fig. 10. The most evident difference after fine-  
 626 tuning is a decrease in the amplitude of the SHAP values. This is because the climato-  
 627 logical rate of positive blocking events in ERA5 is higher: almost 1/3 of nascent blocked  
 628 states persist for 5 d in ERA5, compared to about 1/5 in MM. As the expected fraction

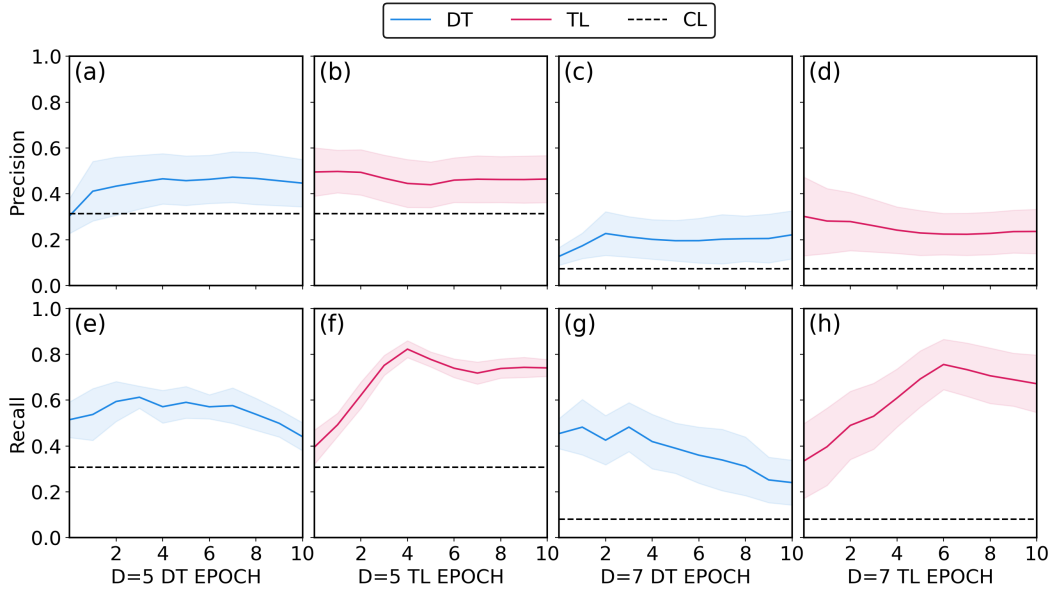


**Figure 8.** Comparison of CNN forecast skill between direct training (DT, blue) and transfer learning (TL, red). Panels (a,b) compare the precision of DT training epoch and of TL fine-tuning epoch for  $D=5$  (standard blocking events). (e,f) compare the recall of DT training epoch and of TL fine-tuning epoch for  $D=5$ . (c,d) compare the same quantities as (a,b) for  $D=7$ . (g,h) compare the same quantities as (e,f) for  $D=7$  (longer blocking events). The black dashed line indicates the climatological event rate  $p$ . The shading shows a two-standard deviation uncertainty bound, as detailed in the text.

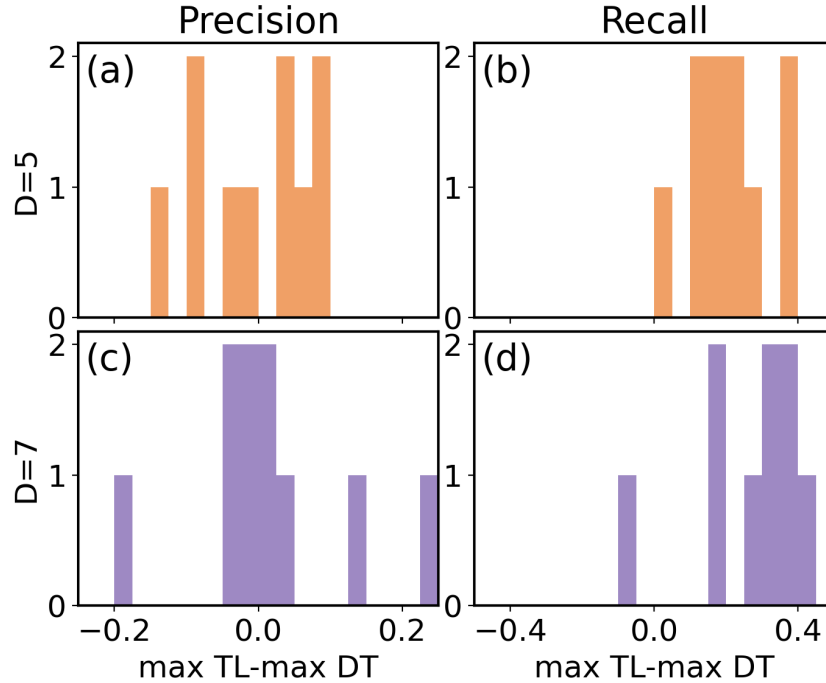


**Figure 9.** Histograms of the performance gap between the best performing CNNs obtained with transfer learning versus the best performing CNNs obtained with direct training, for precision and recall. (a) is the performance gap of precision for 5 d events. (b) is that of recall for 5 d events. (c) and (d) are of precision and recall for 7 d events. “Best performing” was determined by stopping the training procedure at the epoch when the best overall balance between high precision and recall was achieved in the mean (solid lines in Fig. 8). The 90:10 split yields 10 different CNN scores, and the differences between pairs of TL and DT based CNNs, scored on the same test split, are shown.



of events is larger,  $\hat{q}(\mathbf{x}) - \mathbb{E}[\hat{q}(\mathbf{x})]$  from equation (7) will be smaller, and the SHAP value increments  $\phi_i(\hat{q}, \mathbf{x})$  will tend to be smaller. It is the sum of the SHAP values that build up the probability for a  $Y = 1$  prediction; for a more likely event, one does not need to build up the probability as much, so fine-tuning quickly adjusts the weights.

To assess the more subtle change in the relative contribution of each feature on the predicted result after transfer learning, we show the difference in the normalized composite map  $\Delta\phi$  in row  $d$  of Fig. 10.  $\Delta\phi$  is defined for each input  $i$  (i.e., geopotential height  $Z$  at a particular latitude, longitude, and pressure level) by  $\Delta\phi_i \equiv \max\left(\frac{\bar{\phi}_i^{\text{TL}}}{\frac{1}{d} \sum_{j=1}^d \bar{\phi}_j^{\text{TL}}}, 0\right) - \max\left(\frac{\bar{\phi}_i}{\frac{1}{d} \sum_{j=1}^d \bar{\phi}_j}, 0\right)$ . The maximum function is used to avoid spurious negative SHAP values, which should not arise in a composite of true positive events, as discussed in the context of Fig. 5. The normalization makes the total integral of the SHAP values the same for both cases, so that one can focus on where the CNN is using information, as opposed to the overall reduction of the SHAP values driven by the difference in rates.

The “normalized” SHAP values increase mainly in region 4 (the region right around the block), and additionally over Quebec and Atlantic Canada, a region less used for predictions with the MM model. The SHAP values decrease in a relative sense over regions 1 (Florida and the Gulf), 2 (North Atlantic Ocean), 3 (northeastern North America), and central North America. This change in relative importance reveals a general de-emphasis of the regions farther upstream and an increased emphasis on regions more immediately upstream. This indicates that while it is still upstream information that is most important for predicting a persistent blocking state in ERA5, the structure and westward extension of the wave train has changed.

For further insight, we compare the SHAP value patterns with a more traditional method for understanding predictability: composite analysis. Fig. 6 shows composite maps of nascent blocks that evolve into persistent events in the MM model and ERA5. Persistent blocks are associated with wave activity south and west of the blocking region in both the model and reanalysis, but the pattern shifts. The wave train in MM initially arcs westward before turning southward, with a strong center of high pressure east of Florida, while the wave train in ERA5 arcs more to southwest at first, then further westward.

The SHAP values change over Quebec, capturing this shift in the wave train, but overall the CNN seems to shift to more local information with transfer learning. We speculated that the dry, quasi-geostrophic MM model overemphasizes long-range teleconnections. It only captures deformation scale dynamics, and this only at low resolution, and so lacks smaller, local modes of instability, e.g., instability associated with latent heat release due to precipitation, present in our atmosphere. The CNN makes more use of these local features when predicting the persistence of blocks, but still focuses on the upstream flow, consistent with our intuition.

Finally, we contrast the feature importance analysis of the CNN with transfer learning (Fig. 10 row  $b$ ) to that of the CNNs trained only directly on the ERA5 output (Fig. 10 row  $c$ ). DT struggles to develop nuanced features with limited data. The SHAP values with DT are also more barotropic than those with TL. Moreover, in general, the SHAP values with TL capture finer details across a wider spatial range, while the SHAP values with DT are more localized. Geopotential height anomalies over Iceland, especially in the Z500 map, are more emphasized for TL than DT. The same applies to upstream anomalies over Florida and the Gulf of Mexico in the Z200 map. Additionally, the importance of geopotential height anomalies over the Atlantic, immediately upstream of the target region west of north Africa, is neglected in DT, though it appears in TL. This is closely correlated to the blocking event prediction from the ERA5 composite in Fig. 6, which does not show as strong composite Atlantic anomaly as in the MM model.

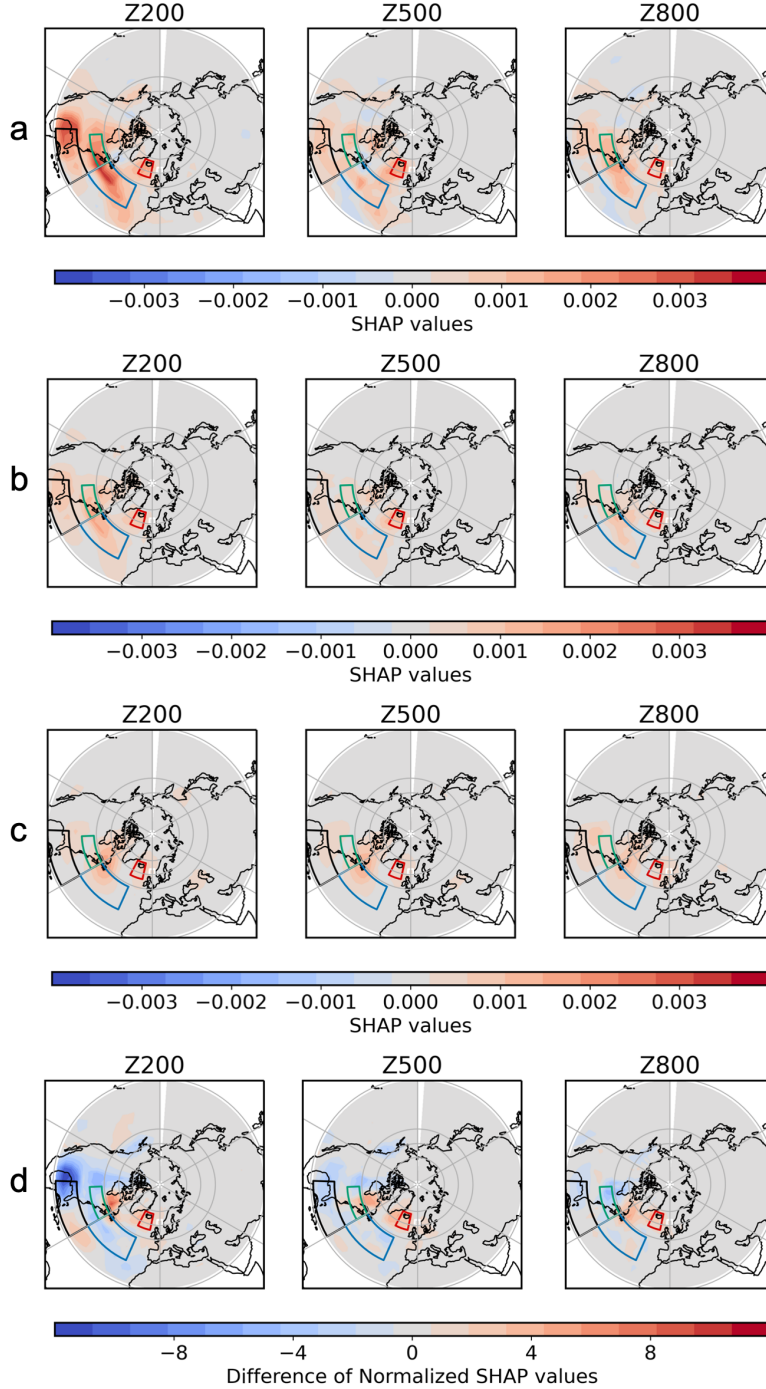


**Figure 10.** Rows 1 through 4 are composite maps of SHAP values,  $\bar{\phi}$ , for geopotential height (200, 500, and 800 hPa), averaged over true positive predictions of blocking events in ERA5 by the CNNs listed below. This is the same quantity shown in Fig.5, but now applied to ERA5 events. Row *a* shows  $\bar{\phi}^{\text{MM}}$  for the pre-trained CNNs before transfer learning (i.e., networks that have only learned from MM, but applied to ERA5). Row *b*:  $\bar{\phi}^{\text{TL}}$  of these pre-trained CNNs after fine-tuning. Row *c*:  $\bar{\phi}^{\text{DT}}$  of CNNs directly trained on ERA5 (i.e., networks that never saw the MM events). Row *d* shows the change in the SHAP values,  $\Delta\phi$ , between the first two rows, after normalization as detailed in the text. This quantifies the effect of transfer learning: positive values indicate that information from the region became more important for the prediction, while negative values indicate that anomalies in the region became less important for prediction.

679 In summary, the superiority of CNNs trained with transfer learning, as compared  
 680 to direct training, appears to lie in their ability to leverage learned features from the pre-  
 681 trained dataset, helping the network to take advantage of information further upstream  
 682 of the blocking region. In either case the precision is modest: when the networks call an  
 683 event, the rate of success is at best 50% higher than a naïve climatological forecast. Pre-  
 684 training the network, however, has a significant impact on the recall, increasing the fore-  
 685 cast rate to capture more events without decreasing the precision.

## 686 8 Conclusion

687 The impact of data-driven science on weather and climate science has grown sub-  
 688 stantially in recent years. In this paper, we suggest two data-driven approaches to help  
 689 predict and understand atmospheric blocking events. First, given sufficient data, con-  
 690 volutional neural networks (CNNs) are capable of identifying subtle features that dif-  
 691 ferentiate short-lived blocked states from those that persist for an extended period. **More-**  
 692 **over, Explainable Artificial Intelligence methods, like SHAP feature importance anal-**  
 693 **ysis, can provide insight into what features matter most to this differentiation.** Second,  
 694 transfer learning has the potential to make data-driven forecasts possible for our atmo-  
 695 sphere, making the most of the limited extreme events in the observational record by lever-  
 696 aging insight from longer, albeit imperfect, numerical simulations.

697 We began in a data-rich regime with the idealized Marshall-Molteni model, show-  
 698 ing that a CNN can accurately predict the persistence of North Atlantic blocks in terms  
 699 of both precision and recall. Leveraging SHAP feature importance analysis, we identi-  
 700 fied crucial regions for the prediction of persistent blocked states, given a nascent high-  
 701 pressure anomaly. Our results suggest that incorporation of both local and non-local fea-  
 702 tures is important for prediction skill.

703 To validate our discovery, we constructed a two-dimensional model that used only  
 704 upstream anomalies over Florida and the Gulf of Mexico, and anomalies immediately  
 705 upstream of the blocking region. The sparse model exhibited precision significantly above  
 706 the climatological rate and recall nearly as good as the full CNN. It struggled, however,  
 707 with false positives (and hence exhibited low precision relative to the CNN) which could  
 708 not be improved within the log linear logistic regression framework. This suggests the  
 709 CNN learns non-trivial relations in the upstream flow, extending all the way to the Pa-  
 710 cific, to better discriminate between short-lived and long-lived blocks.

711 The challenge of conducting direct training on ERA5 data stems from the paucity  
 712 of available events. Small training and test datasets make training and evaluation dif-  
 713 ficult. With the MM model, we observed a systematic degradation in forecast skill when  
 714 the training data was limited, particularly for the recall statistic. Through transfer learn-  
 715 ing, we leverage the abundance of data generated by simplified dynamical models to en-  
 716 hance real-world forecasting. By pre-training a CNN on the MM model dataset and re-  
 717 training the deepest layer on the ERA5 dataset, the recall was improved by 34% com-  
 718 pared to a CNN developed with direct training alone for 5 d events, and over 50% for  
 719 more extreme 7 d events, without any loss of precision.

720 In addition to advancing predictive skill, transfer learning in combination with SHAP  
 721 analysis allowed us to compare the predictive features between weather systems in ERA5  
 722 and the idealized quasigeostrophic model. The bottom row of Fig. 6 reveals biases in the  
 723 MM model, which appears overly dependent on upstream features over Florida and the  
 724 Gulf of Mexico relative to blocks in ERA5. This approach provides a new angle of how  
 725 a machine learning approach could guide the diagnosis and quantification of model bi-  
 726 ases. This said, the success of transfer learning results underscores the MM model’s abil-  
 727 ity, despite its simplicity, to capture features that are important for predicting the per-  
 728 sistence of blocked states in the real world. We believe that greater strides could be made

729 by pre-training on a more advanced climate model, or even hindcasts in the subseasonal-  
 730 to-seasonal (S2S) data set (Vitart et al., 2017; Finkel et al., 2023). We expect our re-  
 731 sults will help inform large-scale efforts to incorporate AI into operational forecasts, such  
 732 as the AIFS model (Lang et al., 2024), which already employs transfer learning in a dif-  
 733 ferent form.

734 The methods presented here are not limited to the context of blocking events, and  
 735 can be generalized to the study of other challenging natural phenomena, especially in  
 736 scenarios where data may be limited, and the potential influencing factors are complex  
 737 (e.g. heat domes (Li et al., 2024)). An immediate future goal is to push further on the  
 738 physical and dynamical mechanisms that causes the differences in prediction mechanisms  
 739 for ERA5 and MM model. Another goal is to adapt the present approach to investigate  
 740 the statistical behavior and mechanisms for the onset of the blocking events.

## 741 Appendix A Marshall-Molteni Model

The Marshall-Molteni (MM) model state is specified by potential vorticity  $q_j$  in three layers of the atmosphere,  $j = 1, 2, 3$ , corresponding to pressure levels 200, 500, and 800 hPa.  $q_j$  evolves according to quasi-geostrophic dynamics as

$$\partial_t q_j + J(\psi_j, q_j) = -D_j + S_j \quad (\text{A1})$$

where  $\psi_j$  is the streamfunction in layer  $j$ , related to  $q_j$  as

$$q_1 = \Delta\psi_1 - (\psi_1 - \psi_2)/R_1^2 + f \quad (\text{A2})$$

$$q_2 = \Delta\psi_2 + (\psi_1 - \psi_2)/R_1^2 - (\psi_2 - \psi_3)/R_2^2 + f \quad (\text{A3})$$

$$q_3 = \Delta\psi_3 + (\psi_2 - \psi_3)/R_2^2 + f(1 + h/H_0). \quad (\text{A4})$$

Here,  $\Delta$  is the horizontal Laplacian operator,  $R_1 = 761$  km and  $R_2 = 488$  km are the Rossby deformation radii in layers 1 and 2,  $f = 2\Omega \cos \phi$  is the latitude-dependent Coriolis parameter, and  $h$  is the orography of the surface, rescaled by the constant  $H_0$ . The operator  $D_j$  combines all dissipative terms, including radiative damping, surface friction and hyper-diffusion to crudely parametrize small scale diffusion, but is also necessary for numerical stability:

$$\begin{aligned} -D_1 &= (\psi_1 - \psi_2)/(\tau_R R_1^2) - R^8 \Delta^4 q_1 / (\tau_H \lambda_{max}^4) \\ -D_2 &= -(\psi_1 - \psi_2)/(\tau_R R_1^2) + (\psi_2 - \psi_3)/(\tau_R R_2^2) - R^8 \Delta^4 q_2' / (\tau_H \lambda_{max}^4) \\ -D_3 &= -(\psi_2 - \psi_3)/(\tau_R R_2^2) - EK_3 - R^8 \Delta^4 q_3' / (\tau_H \lambda_{max}^4). \end{aligned} \quad (\text{A5})$$

The forcing,  $S_j$  is computed from observed data to inject energy into the system and give the model a realistic mean state:

$$S_j = \overline{J(\psi_j, q_j)} + \overline{D_j} \quad (\text{A6})$$

742 The data to construct  $S_j$  were drawn from the 1983–1992 winter (DJF) climatol-  
 743 ogy of the ERA40 reanalysis provided by ECMWF.

## 744 Appendix B Acronyms and definitions

745 Here we list the important acronyms and definitions in this paper for the conve-  
 746 nience of the readers.

- 747 • CNN: Convolutional Neural Network - A type of deep learning model particularly  
 748 effective for analyzing visual data, using convolutional layers to automatically de-  
 749 tect and learn patterns.

- 750 • SHAP: Shapley Additive ExPlanation - A method to explain the output of ma-  
751 chine learning models by attributing contributions of individual features based on  
752 cooperative game theory.
- 753 • MM: Marshall-Molteni - Refers to the 3-layer QG model by (Marshall & Molteni,  
754 1993) related to atmospheric dynamics, often used in the context of studying large-  
755 scale weather patterns and teleconnections.
- 756 • QG: Quasi-Geostrophic - A simplified model in geophysical fluid dynamics that  
757 describes large-scale atmospheric and oceanic flows, assuming a balance between  
758 pressure gradient and Coriolis forces.
- 759 • XAI: Explainable Artificial Intelligence - A subfield of AI focused on making the  
760 outputs and processes of machine learning models transparent and understand-  
761 able to humans.
- 762 • DG: Dole & Gordon index (Dole & Gordon, 1983)- An index developed by Dole  
763 and Gordon to quantify atmospheric blocking events, which are large-scale pres-  
764 sure systems that can disrupt normal weather patterns.
- 765 • DT: Direct Training - A machine learning approach where a model is trained di-  
766 rectly on a specific dataset without additional pre-training or transfer learning tech-  
767 niques.
- 768 • TL: Transfer Learning - A machine learning technique where a pre-trained model  
769 is adapted to a new but related task, leveraging the knowledge gained from the  
770 original task to improve performance.
- 771 •  $Z$ : Geopotential height.
- 772 •  $Z_B(t)$ : Anomalous geopotential height in our target blocking region in the North  
773 Atlantic, shown in Fig. 1.
- 774 •  $T$ : Number of consecutive days of a blocked state.
- 775 •  $M$ : Threshold of geopotential height anomaly in blocking events criteria.
- 776 •  $D$ : Threshold of consecutive days in blocking events criteria.
- 777 •  $\mathbf{X}$ : Full model state vector.
- 778 •  $Y$ : Indicator of whether a blocked state persisted.
- 779 •  $q(\mathbf{x}(t))$ : Conditional probability that a blocked state  $\mathbf{x}(t)$  will persist.
- 780 •  $L(q)$ : Binary cross entropy loss function used for classification problem.
- 781 • Precision:  $\frac{\text{True positives}}{\text{True positives} + \text{False positives}}$
- 782 • Recall:  $\frac{\text{True positives}}{\text{True positives} + \text{False negatives}}$

## 783 Open Research Section

784 The data from the Marshall-Molteni model were generated using a Fortran code  
785 provided by Valerio Lucarini and Andrey Gritsun (Lucarini & Gritsun, 2020). The For-  
786 tran code, along with the Python code for computing SHAP values, transfer learning and  
787 producing plots is publicly available in the the open repository (Zhang, 2024). SHAP  
788 values were computed using the Python package DeepSHAP(Chen, 2022). The ERA5  
789 reanalysis datasets from ECWMF were used for data preprocessing and ML model train-  
790 ing and testing (Hersbach et al., 2020).

## 791 Acknowledgments

792 We thank Valerio Lucarini and Andrey Gritsun for sharing their Marshall-Molteni For-  
793 tran code. We also thank Pedram Hassanzadeh and the anonymous reviewers for many  
794 helpful comments and suggestions that strengthend the paper. This work was supported  
795 by the Army Research Office, grant number W911NF-22-2-0124. EPG acknowledges sup-  
796 port from the National Science Foundation through award OAC-2004572. J. F. is sup-  
797 ported through the MIT Climate Grand Challenge on Weather and Climate Extremes,  
798 and the Virtual Earth Systems Research Institute (VESRI) at Schmidt Sciences.

799

**References**

- 800 Barnes, E. A., & Hartmann, D. L. (2010). Dynamical feedbacks and the persistence of the nao. *Journal of the Atmospheric Sciences*, *67*(3), 851 - 865.  
801 Retrieved from [https://journals.ametsoc.org/view/journals/atsc/67/3/](https://journals.ametsoc.org/view/journals/atsc/67/3/2009jas3193.1.xml)  
802 [2009jas3193.1.xml](https://journals.ametsoc.org/view/journals/atsc/67/3/2009jas3193.1.xml) doi: 10.1175/2009JAS3193.1
- 803 Berckmans, J., Woollings, T., Demory, M.-E., Vidale, P.-L., & Roberts, M. (2013).  
804 Atmospheric blocking in a high resolution climate model: influences of mean  
805 state, orography and eddy forcing. *Atmospheric Science Letters*, *14*(1), 34–40.
- 806 Chan, P.-W., Hassanzadeh, P., & Kuang, Z. (2019). Evaluating Indices of Blocking  
807 Anticyclones in Terms of Their Linear Relations With Surface Hot Extremes.  
808 *Geophysical Research Letters*, *46*(9), 4904-4912. Retrieved from [https://](https://agupubs.onlinelibrary.wiley.com/doi/abs/10.1029/2019GL083307)  
809 [agupubs.onlinelibrary.wiley.com/doi/abs/10.1029/2019GL083307](https://agupubs.onlinelibrary.wiley.com/doi/abs/10.1029/2019GL083307) doi:  
810 <https://doi.org/10.1029/2019GL083307>
- 811 Charney, J. G., & DeVore, J. G. (1979). Multiple flow equilibria in the atmosphere  
812 and blocking. *Journal of Atmospheric Sciences*, *36*(7), 1205–1216.
- 813 Chen, H. (2022, May). *sunleelab/deepshap: Nature communications code [Software]*.  
814 Zenodo. Retrieved from <https://doi.org/10.5281/zenodo.6585445> doi: 10  
815 [.5281/zenodo.6585445](https://doi.org/10.5281/zenodo.6585445)
- 816 Conover, W. J. (1999). *Practical nonparametric statistics* (Vol. 350). john wiley &  
817 sons.
- 818 Davini, P., & D’Andrea, F. (2020). From CMIP3 to CMIP6: Northern Hemisphere  
819 Atmospheric Blocking Simulation in Present and Future Climate. *Journal of*  
820 *Climate*, *33*(23), 10021 - 10038. Retrieved from [https://journals.ametsoc](https://journals.ametsoc.org/view/journals/clim/33/23/jcliD190862.xml)  
821 [.org/view/journals/clim/33/23/jcliD190862.xml](https://journals.ametsoc.org/view/journals/clim/33/23/jcliD190862.xml) doi: [https://doi.org/10](https://doi.org/10.1175/JCLI-D-19-0862.1)  
822 [.1175/JCLI-D-19-0862.1](https://doi.org/10.1175/JCLI-D-19-0862.1)
- 823 Davini, P., & D’Andrea, F. (2016). Northern Hemisphere atmospheric blocking rep-  
824 resentation in global climate models: twenty years of improvements? *Journal*  
825 *of Climate*, *29*(24), 8823–8840.
- 826 Davini, P., Weisheimer, A., Balmaseda, M., Johnson, S. J., Molteni, F., Roberts,  
827 C. D., ... Stockdale, T. N. (2021). The representation of winter northern  
828 hemisphere atmospheric blocking in ecmwf seasonal prediction systems. *Quar-*  
829 *terly Journal of the Royal Meteorological Society*, *147*(735), 1344–1363.
- 830 Dikshit, A., & Pradhan, B. (2021). Explainable AI in drought forecasting. *Ma-*  
831 *chine Learning with Applications*, *6*, 100192. Retrieved from [https://](https://www.sciencedirect.com/science/article/pii/S2666827021000967)  
832 [www.sciencedirect.com/science/article/pii/S2666827021000967](https://www.sciencedirect.com/science/article/pii/S2666827021000967) doi:  
833 <https://doi.org/10.1016/j.mlwa.2021.100192>
- 834 Dole, R. M., & Gordon, N. D. (1983). Persistent anomalies of the extratropical  
835 Northern Hemisphere wintertime circulation: Geographical distribution and  
836 regional persistence characteristics. *Monthly Weather Review*, *111*(8), 1567–  
837 1586.
- 838 d’Andrea, F., Tibaldi, S., Blackburn, M., Boer, G., Déqué, M., Dix, M., ... others  
839 (1998). Northern Hemisphere atmospheric blocking as simulated by 15 atmo-  
840 spheric general circulation models in the period 1979–1988. *Climate Dynamics*,  
841 *14*, 385–407.
- 842 Evans, K. J., & Black, R. X. (2003). Piecewise tendency diagnosis of weather  
843 regime transitions. *Journal of the Atmospheric Sciences*, *60*(16), 1941 -  
844 1959. Retrieved from [https://journals.ametsoc.org/view/journals/](https://journals.ametsoc.org/view/journals/atsc/60/16/1520-0469_2003_060_1941_ptdowr_2.0.co_2.xml)  
845 [atsc/60/16/1520-0469\\_2003\\_060\\_1941\\_ptdowr\\_2.0.co\\_2.xml](https://journals.ametsoc.org/view/journals/atsc/60/16/1520-0469_2003_060_1941_ptdowr_2.0.co_2.xml) doi:  
846 [10.1175/1520-0469\(2003\)060<1941:PTDOWR>2.0.CO;2](https://doi.org/10.1175/1520-0469(2003)060<1941:PTDOWR>2.0.CO;2)
- 847 Ferranti, L., Corti, S., & Janousek, M. (2015). Flow-dependent verification of  
848 the ECMWF ensemble over the Euro-Atlantic sector. *Quarterly Journal*  
849 *of the Royal Meteorological Society*, *141*(688), 916-924. Retrieved from  
850 <https://rmets.onlinelibrary.wiley.com/doi/abs/10.1002/qj.2411>  
851 doi: <https://doi.org/10.1002/qj.2411>
- 852 Finkel, J., Webber, R. J., Gerber, E. P., Abbot, D. S., & Weare, J. (2021). Learn-



- ing Forecasts of Rare Stratospheric Transitions from Short Simulations. *Monthly Weather Review*, 149(11), 3647 - 3669. Retrieved from <https://journals.ametsoc.org/view/journals/mwre/149/11/MWR-D-21-0024.1.xml> doi: <https://doi.org/10.1175/MWR-D-21-0024.1>
- Finkel, J., Webber, R. J., Gerber, E. P., Abbot, D. S., & Weare, J. (2023). Data-Driven Transition Path Analysis Yields a Statistical Understanding of Sudden Stratospheric Warming Events in an Idealized Model. *Journal of the Atmospheric Sciences*, 80(2), 519 - 534. Retrieved from <https://journals.ametsoc.org/view/journals/atsc/80/2/JAS-D-21-0213.1.xml> doi: <https://doi.org/10.1175/JAS-D-21-0213.1>
- González, J. L., Chapman, T., Chen, K., Nguyen, H., Chambers, L., Mostafa, S. A., ... Yue, J. (2022). Atmospheric Gravity Wave Detection Using Transfer Learning Techniques. In *2022 IEEE/ACM International Conference on Big Data Computing, Applications and Technologies (BDCAT)* (p. 128-137). doi: 10.1109/BDCAT56447.2022.00023
- Goodfellow, I., Bengio, Y., & Courville, A. (2016). *Deep learning*. MIT Press. (<http://www.deeplearningbook.org>)
- Guo, Y., Wu, X., Qing, C., Su, C., Yang, Q., & Wang, Z. (2022). Blind Restoration of Images Distorted by Atmospheric Turbulence Based on Deep Transfer Learning. *Photonics*, 9(8). Retrieved from <https://www.mdpi.com/2304-6732/9/8/582> doi: 10.3390/photonics9080582
- Ham, Y.-G., Kim, J.-H., & Luo, J.-J. (2019, Sep 01). Deep learning for multi-year ENSO forecasts. *Nature*, 573(7775), 568-572. Retrieved from <https://doi.org/10.1038/s41586-019-1559-7> doi: 10.1038/s41586-019-1559-7
- Hersbach, H., Bell, B., Berrisford, P., Hirahara, S., Horányi, A., Muñoz-Sabater, J., ... Thépaut, J.-N. (2020). The era5 global reanalysis. *Quarterly Journal of the Royal Meteorological Society*, 146(730), 1999-2049. Retrieved from <https://rmets.onlinelibrary.wiley.com/doi/abs/10.1002/qj.3803> doi: <https://doi.org/10.1002/qj.3803>
- Hoskins, B. J., James, I. N., & White, G. H. (1983, July). The Shape, Propagation and Mean-Flow Interaction of Large-Scale Weather Systems. *Journal of Atmospheric Sciences*, 40(7), 1595-1612. doi: 10.1175/1520-0469(1983)040<1595:TSPAMF>2.0.CO;2
- Hussain, M., Bird, J. J., & Faria, D. R. (2019). A study on cnn transfer learning for image classification. In *Advances in Computational Intelligence Systems: Contributions Presented at the 18th UK Workshop on Computational Intelligence, September 5-7, 2018, Nottingham, UK* (pp. 191-202).
- Jacques-Dumas, V., Ragone, F., Borgnat, P., Abry, P., & Bouchet, F. (2022). Deep learning-based extreme heatwave forecast. *Frontiers in Climate*, 4.
- Jacques-Dumas, V., van Westen, R. M., Bouchet, F., & Dijkstra, H. A. (2023). Data-driven methods to estimate the committor function in conceptual ocean models. *Nonlinear Processes in Geophysics*, 30(2), 195-216. Retrieved from <https://npg.copernicus.org/articles/30/195/2023/> doi: 10.5194/npg-30-195-2023
- Johnson, J. M., & Khoshgoftaar, T. M. (2019). Survey on deep learning with class imbalance. *Journal of Big Data*, 6(1), 1-54.
- Kautz, L.-A., Martius, O., Pfahl, S., Pinto, J. G., Ramos, A. M., Sousa, P. M., & Woollings, T. (2022). Atmospheric blocking and weather extremes over the Euro-Atlantic sector – a review. *Weather and Climate Dynamics*, 3(1), 305-336. Retrieved from <https://wcd.copernicus.org/articles/3/305/2022/> doi: 10.5194/wcd-3-305-2022
- Labe, Z. M., & Barnes, E. A. (2021). Detecting Climate Signals Using Explainable AI With Single-Forcing Large Ensembles. *Journal of Advances in Modeling Earth Systems*, 13(6), e2021MS002464. Retrieved from <https://agupubs.onlinelibrary.wiley.com/doi/abs/10.1029/>



- 2021MS002464 (e2021MS002464 2021MS002464) doi: <https://doi.org/10.1029/2021MS002464>
- Lang, S., Alexe, M., Chantry, M., Dramsch, J., Pinault, F., Raoult, B., ... Rabier, F. (2024). *Aifs - ecmwf's data-driven forecasting system*. Retrieved from <https://arxiv.org/abs/2406.01465>
- Li, X., Mann, M. E., Wehner, M. F., Rahmstorf, S., Petri, S., Christiansen, S., & Carrillo, J. (2024). Role of atmospheric resonance and land-atmosphere feedbacks as a precursor to the June 2021 Pacific Northwest heat dome event. *Proceedings of the National Academy of Sciences*, *121*(4), e2315330121. Retrieved from <https://www.pnas.org/doi/abs/10.1073/pnas.2315330121> doi: 10.1073/pnas.2315330121
- Linardatos, P., Papastefanopoulos, V., & Kotsiantis, S. (2020). Explainable ai: A review of machine learning interpretability methods. *Entropy*, *23*(1), 18.
- Lipovetsky, S., & Conklin, M. (2001). Analysis of regression in game theory approach. *Applied Stochastic Models in Business and Industry*, *17*(4), 319-330. Retrieved from <https://onlinelibrary.wiley.com/doi/abs/10.1002/asmb.446> doi: <https://doi.org/10.1002/asmb.446>
- Liu, Y., Racah, E., Prabhat, Correa, J., Khosrowshahi, A., Lavers, D., ... Collins, W. (2016). *Application of Deep Convolutional Neural Networks for Detecting Extreme Weather in Climate Datasets*.
- Lucarini, V., & Gritsun, A. (2020). A new mathematical framework for atmospheric blocking events. *Climate Dynamics*, *54*(1-2), 575-598.
- Lucente, D., Herbert, C., & Bouchet, F. (2022). Commitor functions for climate phenomena at the predictability margin: The example of El Niño southern oscillation in the Jin and Timmermann model. *Journal of the Atmospheric Sciences*. Retrieved from <https://journals.ametsoc.org/view/journals/atsc/aop/JAS-D-22-0038.1/JAS-D-22-0038.1.xml> doi: 10.1175/JAS-D-22-0038.1
- Lundberg, S. M., & Lee, S.-I. (2017). A unified approach to interpreting model predictions. *Advances in neural information processing systems*, *30*.
- Lupo, A. R. (2021). Atmospheric blocking events: a review. *Annals of the New York Academy of Sciences*, *1504*(1), 5-24. Retrieved from <https://nyaspubs.onlinelibrary.wiley.com/doi/abs/10.1111/nyas.14557> doi: <https://doi.org/10.1111/nyas.14557>
- Lupo, A. R., Mokhov, I. I., Akperov, M. G., Chernokulsky, A. V., Athar, H., et al. (2012). A dynamic analysis of the role of the planetary- and synoptic-scale in the summer of 2010 blocking episodes over the European part of Russia. *Advances in Meteorology*, *2012*.
- Malmgren-Hansen, D., Nielsen, A. A., Laparra, V., & Valls, G. C. (2018). Transfer Learning with Convolutional Networks for Atmospheric Parameter Retrieval. In *IGARSS 2018 - 2018 IEEE International Geoscience and Remote Sensing Symposium* (p. 2111-2114). doi: 10.1109/IGARSS.2018.8518097
- Marshall, J., & Molteni, F. (1993). Toward a dynamical understanding of planetary-scale flow regimes. *Journal of the Atmospheric Sciences*, *50*(12), 1792-1818.
- Matsueda, M. (2009). Blocking Predictability in Operational Medium-Range Ensemble Forecasts. *SOLA*, *5*, 113-116. doi: 10.2151/sola.2009-029
- McWilliams, J. C. (1980). An application of equivalent modons to atmospheric blocking. *Dynamics of Atmospheres and Oceans*, *5*(1), 43-66. Retrieved from <https://www.sciencedirect.com/science/article/pii/037702658090010X> doi: [https://doi.org/10.1016/0377-0265\(80\)90010-X](https://doi.org/10.1016/0377-0265(80)90010-X)
- Michelangeli, P.-A., & Vautard, R. (1998). The dynamics of Euro-Atlantic blocking onsets. *Quarterly Journal of the Royal Meteorological Society*, *124*(548), 1045-1070.
- Miloshevich, G., Cozian, B., Abry, P., Borgnat, P., & Bouchet, F. (2023, Apr). Probabilistic forecasts of extreme heatwaves using convolutional neural net-

- 964 works in a regime of lack of data. *Phys. Rev. Fluids*, 8, 040501. Retrieved  
 965 from <https://link.aps.org/doi/10.1103/PhysRevFluids.8.040501> doi:  
 966 10.1103/PhysRevFluids.8.040501
- 967 Mu, B., Ma, S., Yuan, S., & Xu, H. (2020). Applying convolutional lstm net-  
 968 work to predict el niño events: Transfer learning from the data of dynamical  
 969 model and observation. In *2020 IEEE 10th International Conference on Elec-  
 970 tronics Information and Emergency Communication (ICEIEC)* (p. 215-219). doi:  
 971 10.1109/ICEIEC49280.2020.9152317
- 972 Mullen, S. L. (1987). Transient eddy forcing of blocking flows. *Journal of the Atmo-  
 973 spheric Sciences*, 44(1), 3–22.
- 974 Pelly, J. L., & Hoskins, B. J. (2003). A new perspective on blocking. *Journal of the  
 975 atmospheric sciences*, 60(5), 743–755.
- 976 Rampal, N., Gibson, P. B., Sood, A., Stuart, S., Fauchereau, N. C., Brandolino,  
 977 C., ... Meyers, T. (2022). High-resolution downscaling with interpretable  
 978 deep learning: Rainfall extremes over New Zealand. *Weather and Climate  
 979 Extremes*, 38, 100525. Retrieved from [https://www.sciencedirect.com/  
 980 science/article/pii/S2212094722001049](https://www.sciencedirect.com/science/article/pii/S2212094722001049) doi: [https://doi.org/10.1016/  
 981 j.wace.2022.100525](https://doi.org/10.1016/j.wace.2022.100525)
- 982 Rasp, S., & Thuerey, N. (2021). Data-Driven Medium-Range Weather Predic-  
 983 tion With a Resnet Pretrained on Climate Simulations: A New Model for  
 984 WeatherBench. *Journal of Advances in Modeling Earth Systems*, 13(2),  
 985 e2020MS002405. Retrieved from [https://agupubs.onlinelibrary.wiley  
 986 .com/doi/abs/10.1029/2020MS002405](https://agupubs.onlinelibrary.wiley.com/doi/abs/10.1029/2020MS002405) (e2020MS002405 2020MS002405) doi:  
 987 <https://doi.org/10.1029/2020MS002405>
- 988 Rex, D. F. (1950). Blocking Action in the Middle Troposphere and its Effect  
 989 upon Regional Climate. *Tellus*, 2(3), 196-211. Retrieved from [https://  
 990 onlinelibrary.wiley.com/doi/abs/10.1111/j.2153-3490.1950.tb00331.x](https://onlinelibrary.wiley.com/doi/abs/10.1111/j.2153-3490.1950.tb00331.x)  
 991 doi: <https://doi.org/10.1111/j.2153-3490.1950.tb00331.x>
- 992 Rudy, S. H., & Sapsis, T. P. (2023). Output-weighted and relative entropy loss  
 993 functions for deep learning precursors of extreme events. *Physica D: Nonlinear  
 994 Phenomena*, 443, 133570.
- 995 Sasaki, Y., et al. (2007). The truth of the f-measure. 2007. URL: [https://www. cs.  
 996 odu. edu/mukka/cs795sum09dm/Lecturenotes/Day3/F-measure-YS-26Oct07.  
 997 pdf \[accessed 2021-05-26\]](https://www.cs.odu.edu/mukka/cs795sum09dm/Lecturenotes/Day3/F-measure-YS-26Oct07.pdf), 49.
- 998 Scaife, A. A., Woollings, T., Knight, J., Martin, G., & Hinton, T. (2010). Atmo-  
 999 spheric blocking and mean biases in climate models. *Journal of Climate*,  
 1000 23(23), 6143–6152.
- 1001 Shrikumar, A., Greenside, P., & Kundaje, A. (2017). Learning important features  
 1002 through propagating activation differences. In *International conference on ma-  
 1003 chine learning* (pp. 3145–3153).
- 1004 Shutts, G. (1983). The propagation of eddies in diffluent jetstreams: Eddy vortic-  
 1005 ity forcing of ‘blocking’ flow fields. *Quarterly Journal of the Royal Meteorologi-  
 1006 cal Society*, 109(462), 737–761.
- 1007 Silva, S. J., Keller, C. A., & Hardin, J. (2022). Using an explainable machine  
 1008 learning approach to characterize Earth System model errors: Application of  
 1009 SHAP analysis to modeling lightning flash occurrence. *Journal of Advances in  
 1010 Modeling Earth Systems*, 14(4), e2021MS002881.
- 1011 Subel, A., Chattopadhyay, A., Guan, Y., & Hassanzadeh, P. (2021). Data-driven  
 1012 subgrid-scale modeling of forced Burgers turbulence using deep learning with  
 1013 generalization to higher Reynolds numbers via transfer learning. *Physics of  
 1014 Fluids*, 33(3).
- 1015 Taló, M., Baloglu, U. B., Yıldırım, Ö., & Acharya, U. R. (2019). Application of  
 1016 deep transfer learning for automated brain abnormality classification using MR  
 1017 images. *Cognitive Systems Research*, 54, 176–188.
- 1018 Tantet, A., van der Burgt, F. R., & Dijkstra, H. A. (2015). An early warning in-

- 1019           indicator for atmospheric blocking events using transfer operators. *Chaos: An*  
1020 *Interdisciplinary Journal of Nonlinear Science*, 25(3), 036406. Retrieved from  
1021 <https://doi.org/10.1063/1.4908174> doi: 10.1063/1.4908174
- 1022 Tibaldi, S., & Molteni, F. (1990). On the operational predictability of blocking. *Tel-*  
1023 *lus A*, 42(3), 343–365.
- 1024 Vitart, F., Ardilouze, C., Bonet, A., Brookshaw, A., Chen, M., Codorean, C., ...  
1025 Zhang, L. (2017). The Subseasonal to Seasonal (S2S) Prediction Project  
1026 Database. *Bulletin of the American Meteorological Society*, 98(1), 163 - 173.  
1027 Retrieved from [https://journals.ametsoc.org/view/journals/bams/98/1/](https://journals.ametsoc.org/view/journals/bams/98/1/bams-d-16-0017.1.xml)  
1028 [bams-d-16-0017.1.xml](https://journals.ametsoc.org/view/journals/bams/98/1/bams-d-16-0017.1.xml) doi: 10.1175/BAMS-D-16-0017.1
- 1029 Woollings, T., Barriopedro, D., Methven, J., Son, S.-W., Martius, O., Harvey, B., ...  
1030 Seneviratne, S. (2018, Sep 01). Blocking and its Response to Climate Change.  
1031 *Current Climate Change Reports*.
- 1032 Yang, M., Luo, D., Li, C., Yao, Y., Li, X., & Chen, X. (2021). Influ-  
1033 ence of Atmospheric Blocking on Storm Track Activity Over the  
1034 North Pacific During Boreal Winter. *Geophysical Research Let-*  
1035 *ters*, 48(17), e2021GL093863. Retrieved 2023-08-03, from [https://](https://onlinelibrary.wiley.com/doi/abs/10.1029/2021GL093863)  
1036 [onlinelibrary.wiley.com/doi/abs/10.1029/2021GL093863](https://onlinelibrary.wiley.com/doi/abs/10.1029/2021GL093863) (\_eprint:  
1037 <https://onlinelibrary.wiley.com/doi/pdf/10.1029/2021GL093863>) doi:  
1038 10.1029/2021GL093863
- 1039 Yosinski, J., Clune, J., Bengio, Y., & Lipson, H. (2014). How transferable are fea-  
1040 tures in deep neural networks? *Advances in neural information processing sys-*  
1041 *tems*, 27.
- 1042 Zappa, G., Masato, G., Shaffrey, L., Woollings, T., & Hodges, K. (2014a). Linking  
1043 Northern Hemisphere blocking and storm track biases in the CMIP5 climate  
1044 models. *Geophysical Research Letters*, 41(1), 135–139.
- 1045 Zappa, G., Masato, G., Shaffrey, L., Woollings, T., & Hodges, K. (2014b). Linking  
1046 Northern Hemisphere blocking and storm track biases in the CMIP5 climate  
1047 models. *Geophysical Research Letters*, 41(1), 135–139. Retrieved 2023-08-02,  
1048 from <https://onlinelibrary.wiley.com/doi/abs/10.1002/2013GL058480>  
1049 (\_eprint: <https://onlinelibrary.wiley.com/doi/pdf/10.1002/2013GL058480>) doi:  
1050 10.1002/2013GL058480
- 1051 Zhang, H. (2024, September). *hzhang-math/blockingshaptl: Code\_blocking*. Zen-  
1052 odo. Retrieved from <https://doi.org/10.5281/zenodo.13829703> doi: 10  
1053 .5281/zenodo.13829703